Ben-Gurion University of the Negev
The Faculty of Computer and Information Science
The Information Systems Engineering Program

Quantitative analysis of metallomics bioimaging in Triple Negative Breast Cancer patients

Thesis submitted in partial fulfillment of the requirements
for the Master of Sciences degree

Mark Oulitin

Under the supervision of

Prof. Assaf Zaritsky and Dr. Orit Kliper Gross

October 2025

Ben-Gurion University of the Negev
The Faculty of Computer and Information Science
The Information Systems Engineering Program

Quantitative analysis of metallomics bioimaging in Triple Negative Breast Cancer patients

Thesis submitted in partial fulfillment of the requirements
for the Master of Sciences degree

Mark Oulitin

Under the supervision of

Prof. Assaf Zaritsky and Dr. Orit Kliper Gross

Author: Date: 01/10/2025

Supervisor: Date: 01/10/2025

Chairman of Graduate Studies Committee: _____ Date: _____

October 2025

Abstract

Metals play a critical role in cancer biology, yet current analyses rely on bulk measurements or qualitative observations and thus lack spatial quantification. In this thesis, I present a systematic computational pipeline for quantitative spatial metallomics analysis and apply it to predict Neoadjuvant chemotherapy (NACT) response in Triple-Negative Breast Cancer (TNBC) patients. Using Laser Ablation Inductively Coupled Plasma Mass Spectrometry (LA-ICP-MS) imaging, of magnesium, iron, copper, and zinc, in pretreatment core biopsy TNBC tissue samples, our pipeline transforms spatial metallic readouts into histogram-based features that serve as inputs for machine learning models predictive of NACT-response. We demonstrate that the spatial distributions of all four metals contain predictive information for NACT response and identify tissue subregions with high metal concentrations, that we term "hotspots", that play a key role in these predictions. These hotspots partially align with pathological annotations such as tumor, inflammation and fibrous stroma regions, suggesting that they contribute to biologically meaningful regions. While models based on single metals are predictive, we demonstrate that aggregating their predictions enhances the classification of patient response, which further underscores the value of integrating spatial, multi-metal information to uncover predictive biomarkers in TNBC. Altogether, my thesis provides a computational pipeline for quantitative analysis of spatial metallomic bioimaging and demonstrates the importance of multimetal hotspots as informative regions for predicting treatment response.

Acknowledgments

First and foremost, I would like to express my gratitude to my supervisor Prof. Assaf Zaritsky for his constructive criticism and patience throughout my dissertation. I would also like to thank Dr. Orit Kliper-Gross from the Ben-Gurion University of the Negev, for standing by my side with a lot of patience and excitement to conduct new experiments, ask the right questions and provide knowledge. I would also like to thank our collaborators Dr. Alex Morrell and Maddy Parsons team from King's College London for their invaluable contribution in collection, imaging and initial preparation of the data that was a cornerstone for the analysis and results of this research project. I would also like to thank David Goggins, whose story and adventure inspired me to finish my dissertation despite the difficulties and to become a better version of myself.

Contents

List of Figures & Tables

Introduction

Metals are integral to the human body. They participate in numerous physiological processes. For example, iron and copper are essential for the process of oxygen transport [1], [2], zinc is coupled to electrophysiological activity of neurons [3], and magnesium regulates fundamental functions such as muscle contraction, neuromuscular conduction and blood pressure [4]. Imbalanced metal concentration can lead to severe health disorders [1], [2], [3], [4]. For example, an excessive copper deposition in the liver (also known as Wilson disease) can be fatal if untreated [5], an iron overload, related to decrease in immune cells response, reduces the body's ability to fight diseases [6]. There is extensive evidence about the interplay between metals and tumor related processes such as tumor metastasis [7], [8], [9], [10], angiogenesis [10], [11], and cell proliferation [8], [10], [12], [13]. For instance, iron was shown to act as a catalyst in cancer metabolism and fuels tumor growth [14], while blocking copper delivery was related to Triple Negative Breast Cancer (TNBC) cells' death and is known to prevent blood vessel formation which supports tumor development [15]. Additionally, zinc is considered to be a cofactor in the process of DNA damage [16], and magnesium deficiency has been shown to promote breast cancer metastasis [17].

Physiological understanding of the role of metals in cancer development and suppression relies on the ability to measure and quantify metals within tissue samples. Current studies typically perform bulk metal measurements of the tissue, meaning they assess average metal concentrations across pooled populations of cells without resolving cellular or spatial heterogeneity. The tissue's bulk metal measurements are performed using technologies called "Inductively Coupled Plasma Mass Spectrometry" (ICP-MS) or "Inductively Coupled Plasma Optical Emission Spectroscopy" (ICP-OES) that involve digesting the tissue into a liquid form, introducing it into a high-temperature plasma to ionize the elements, and then detecting and quantifying the metal ions based on their mass-to-charge ratio or optical emission spectra [18]. Using these technologies, Toker et al. have found that blood samples from breast cancer patients contain higher levels of sodium and potassium compared to those of healthy people [19]. Analysis of zinc, copper, iron and magnesium in hair samples conducted by Czerny et al. with ICP-MS and ICP-OES revealed lower concentrations of these elements in cancer patients compared to non cancer patients [20]. Ghezzi et al. used ICP-MS to measure how breast cancer cells absorb different platinum based chemotherapy drugs. They found that the drugs passively diffuse into the cells rather than being actively transported [21]. While bulk metal measurements are useful for measuring overall metal content, they average the spatial heterogeneity within the tissue. This spatial heterogeneity is critical for understanding the mechanistic roles of metals in breast cancer biology, as metal distributions within tissues can reveal microenvironmental characteristics and localized changes between tissue samples with different breast cancer state progression.

To address this need for spatial context we can use Laser Ablation Inductively Coupled Plasma Mass Spectrometry (LA-ICP-MS), an advanced technique that combines laser ablation (to sample material from a solid surface) with ICP-MS (to ionize and analyze the elemental composition), allowing for spatially resolved metal analysis. LA-ICP-MS acquires

spatial metal images of tissue samples by measuring the metal ions mass at each spatial location during the laser ablation pass over the tissue sample [22]. Current LA-ICP-MS analysis typically rely on biologist experts annotations of specific tissue subregions (e.g., tumor vs non-tumor) [23], followed by statistical comparison of metal distribution across these annotated regions [24], [25], [26], or examining the entire tissue metal map in relation to Hematoxylin and Eosin (H&E) staining [24], [25], [26]. For instance, Rusch et al. found within tumor tissue samples a high accumulation of zinc levels with the increase of histopathological grade of malignancy through statistical comparison of pooled pixels from expert selected subregions [25]. Escudero-Cernuda et al. mapped multiple elements (iron, copper, zinc, strontium and barium) and found higher levels of these elements in breast tumor areas compared to stroma, but this required prior tumor localization on H&E images and statistical testing of pooled pixels [26]. The analyses were based on prior expert knowledge or intuition, which drived the research hypothesis. Such qualitative or semi-quantitative analyses workflows can not be applied to large scale tissue sample cohorts, and can not discover patterns that were not pre-defined by the human annotator.

In this thesis, I have focused on establishing a systematic quantitative workflow for spatial multi-metal analysis, exemplifying it within the context of predicting TNBC patient's response to Neoadjuvant chemotherapy (NACT) by leveraging the LA-ICP-MS TNBC cohort (70 core biopsy samples) collected through the Δ-Tissue project [27]. This Single-Arm Prospective cohort contains LA-ICP-MS metal maps of magnesium, iron, copper and zinc alongside an H&E image with pathologist annotations. I present a treatment response classification pipeline of a TNBC patient pretreatment sample. While the pipeline is applied independently on each sample's metal channel (magnesium, iron, copper, and zinc) to train a predictive model, it takes into account multi-metal information during the pre-processing steps. Initially, the pipeline removes "background pixels", defined as low intensity readout across all measured metal channels. Subsequently, it excludes pixels with high metal concentration in all metals, termed as "outlier pixels", which are characteristic of technical noise like salt-and-pepper noise artifacts. Following this background and outlier pixels removal, a histogram-based representation of pixel intensities is constructed for each individual metal and is used to train a treatment response classifier. I demonstrate that the spatial readouts of magnesium, iron, copper, and zinc each independently carry a predictive signal for NACT response. My findings show that this predictive signal is associated with pixels characterized by high intensity in at least one, but not all, metal channels. I termed these pixels as "hotspot pixels". The "hotspot" pixels are clustered together at coherent tissue subregions and partially align with pathological annotations such as tumor areas, inflammation and fibrous stroma regions. This alignment shows the potential of hotspots to capture biologically meaningful features relevant to treatment outcome. Additionally, to further enhance the discriminative signal of this single metal histogram-based representation, two approaches are incorporated. First, "magnitude encoding" features contextualize each sample's intensity distribution relative to the broader cohort measured range, thereby capturing information about absolute intensity. Second, a Yeo-Johnson transformation [28] is applied to the single metal pixel distribution before constructing metal's histogram, this mitigates data skewness while preserving the predictive signal contained within the hotspot

regions. Finally, aggregating predictions of these independent single-metal models led to better prediction of treatment response. Altogether, my thesis provides a computational pipeline for quantitative analysis of spatial multi metallomic bioimaging and demonstrates it on TNBC patient treatment response prediction.

Related Work

My thesis lies within the domains of computational biology and metallomics, a research field which focuses on the role of metals in biological systems. Specifically, my thesis presents a pipeline for quantitative analysis of spatial metallomics that is applied to examine the relationship between the spatial localization of metals and the response of TNBC patients to neoadjuvant chemotherapy.

The roles of metals in breast cancer

Metals are increasingly recognized for their functional role in breast cancer. Iron and magnesium were shown to affect cancer metabolism and tumor growth [14], [29]. Copper is also required for key processes of cancer progression such as proliferative immortality and metastasis [30]. Copper homeostasis-related genes are associated with breast cancer prognosis, with lower copper related gene expression correlating with better survival outcome [31]. Copper homeostasis-related long non-coding RNAs were identified as prognostic biomarkers, with high-risk gene signatures correlating with poorer clinical outcomes in breast cancer patients [32]. A copper-dependent redox protein was shown to play a role in breast cancer cell migration and metastasis, by increasing intracellular reactive oxygen species levels [33]. Elevated serum copper/zinc ratio at diagnosis was associated with poorer survival in breast cancer patients, suggesting that the balance between these elements provides predictive value for patient outcomes [34]. Blocking copper delivery leads to TNBC cells' death and was shown to be involved in stopping the growth of blood vessels that feed the tumor [15], [29], [30]. Zinc was shown to be involved in TNBC invasion and colonisation in healthy tissue [35]. Metallic nanoparticles, including iron oxide, zinc and copper demonstrate therapeutic potential in TNBC by enabling targeted drug delivery [36]. Collectively, these studies highlight the multifaceted roles of metals in breast cancer progression and specifically in TNBC progression, underscoring the importance of getting a better understanding of the interplay between metals and breast cancer.

Metal measurement techniques from patient's samples

One of the first instrumental techniques for bulk measurement of metallic elements in organic materials is atomic absorption spectroscopy (AAS) [37]. While AAS remains a widely used method for elemental analysis, other common techniques rely on Inductively Coupled Plasma (ICP). Inductively Coupled Plasma Atomic Emission Spectroscopy (ICP-AES) (also known as ICP-OES) requires less preparation and analysis time and enables the simultaneous measurement of multiple elements within the same sample [38]. Furthermore, Inductively Coupled Plasma Mass Spectrometry (ICP-MS) offers increased multi-element measurement

capability and higher resolution data [39]. It should be noted that while ICP-based methods provide enhanced measurements compared to AAS, they are typically associated with higher operating and equipment costs.

These methods provide bulk metal readouts, but fail to capture how metals are distributed across distinct tissue regions. As such, recent efforts have turned to LA-ICP-MS, an imaging-based method to visualize and analyze metals spatially. LA-ICP-MS enables high-resolution mapping of trace elements in tissue sections (on the order of a few micrometers) [26], and potentially is able to reveal informative metallic heterogeneity that bulk methods overlook.

Spatial metallomic bioimage analysis using LA-ICP-MS in breast cancer

Early studies demonstrated the effectiveness of LA-ICP-MS technique in conducting spatial analysis within the context of breast cancer. For instance, de Vega et al. [23] applied LA-ICP-MS to test the hypothesis proposed by Kenyon et al. [40], who used bulk measurement of cellular metabolic activity and suggested that copper is essential for cell migration that can lead to cancer metastasis. The LA-ICP-MS imaging analysis by de Vega et al. [23] revealed locally elevated copper levels in carcinoma tissue areas, thereby providing spatial readout evidence supporting Kenyon et al.'s hypothesis.

Rusch et al. [25] showed elevation of zinc concentration in LA-ICP-MS with the increase of the histopathological grade of malignancy. Escudero-Cernuda et al. employed LA-ICP-MS to map iron, copper, zinc, strontium and barium. They found that the levels of these elements are higher in breast tumor niche areas compared to stroma [26]. Riesop et al. found high zinc levels in tumor regions compared to normal stroma using LA-ICP-MS imaging [24]. Doble et al. found that manganese levels in tumor regions appear to correlate with radiation resistance [41]. Such results exemplify the value of LA-ICP-MS imaging for qualitative analysis of metals. However, these early studies focus on manually annotating subregions [23] and comparing the aggregated metal levels using simple statistical tests and visual comparison against H&E image [24], [25]. Despite its proven capabilities, the potential of LA-ICP-MS for systematic and large-scale quantitative analysis of spatial metal distributions is yet underexplored.

Research Objectives

The primary objective of this thesis is to move beyond the limitations of bulk measurements and qualitative visual assessments of spatial metal distributions. We achieve this goal by establishing a systematic and quantitative computational pipeline for spatial metallomic analysis. By leveraging high-resolution LA-ICP-MS imaging, we exemplify this systematic workflow in pretreatment tissue samples in analysis of spatial heterogeneity of metals and evaluation them as predictive biomarkers for Neoadjuvant Chemotherapy (NACT) response in Triple Negative Breast Cancer (TNBC) patients. The results of this analysis and evaluation are then manually verified in comparison to matched H&E-stained images to drive a biological interpretation of the results.

Results

Treatment response prediction pipeline of metallomics bioimaging

We used a TNBC patients tissue samples cohort collected by our collaborators from Maddy's Parsons team in King's College London as part of the Δ-Tissue project. This Single-Arm Prospective cohort includes 70 'core' biopsy tissue samples collected from 66 TNBC patients before neoadjuvant chemotherapy (NACT) (Fig. 1A). Based on treatment response, each patient was classified as either a 'responder' (pathological complete response) or 'non-responder' pathologically (Fig. 1A-B). We analyzed two matched sections from the same tissue, imaged 12 µm apart. The first section was H&E-stained and partially annotated, with detailed pathologist-annotations for 21 out of 70 tissue sections. The matching section was imaged by LA-ICP-MS for magnesium, iron, copper, and zinc (Fig. 1C). Each pixel intensity in the LA-ICP-MS metal map represents a metal readout in µg/g units with a pixel resolution of 20 µm. The tissue segmentation mask was acquired from scanning the tissue sample at predefined key points. The LA-ICP-MS data was acquired and calibrated using certified reference materials by our collaborator, Dr. Alex Morrell (Methods).

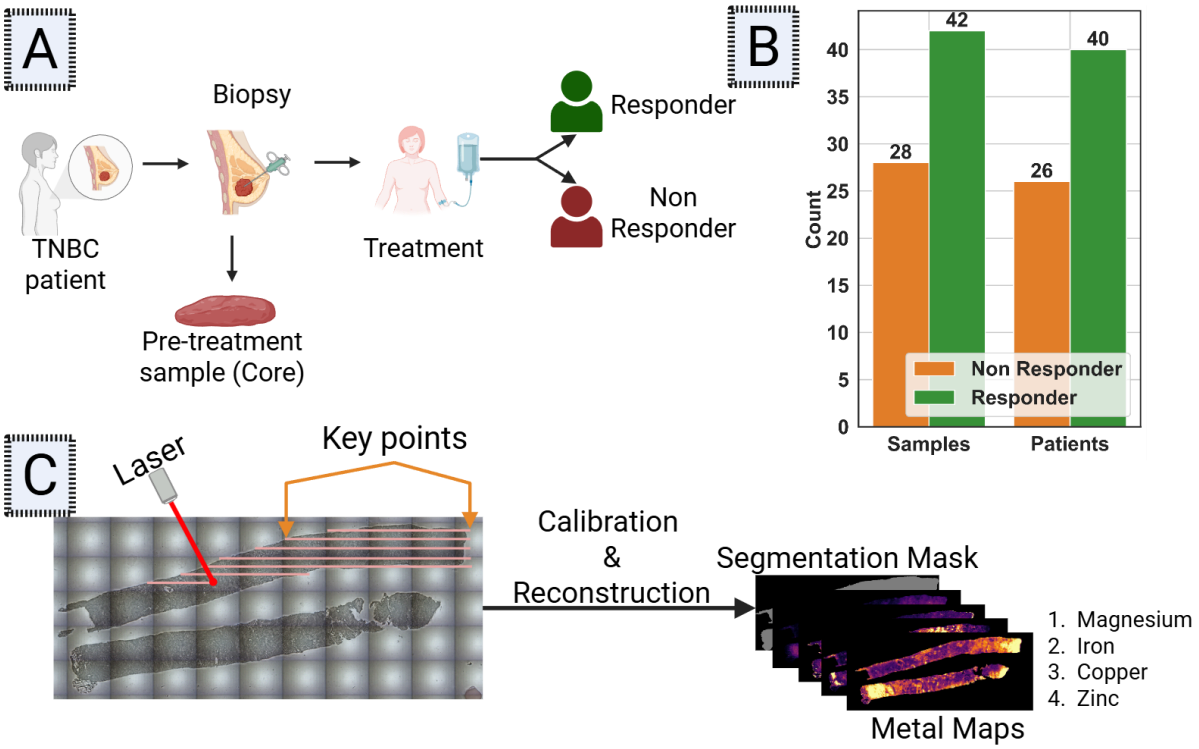

Figure 1. (**A**) Overview of tissue sample collection and patient classification into responder (pathological complete response) and non-responder groups after NACT treatment. (**B**) Distribution of responder vs. non-responder at patient and sample levels, illustrating dataset imbalance. (**C**) LA-ICP-MS imaging process: laser ablation in a raster scan between predefined key points over an optical image of the tissue. The raw data was calibrated and reconstructed into a 2D image of magnesium, iron, copper, and zinc channels.

Using this data, we first examined if metal "bulk" measurements are predictive biomarkers of treatment response. We simulated a metal bulk readout from the spatial metal image by averaging the metal intensities, per sample, over all the pixels. Then, for each metal, we conducted a t-test over these bulk measurements to separate between responder and non-responder tissue samples. Our simulated bulk readout didn't reveal a discriminative signal (Fig. 2A).

Hypothesizing that the metal heterogeneity within the tissue section could discriminate between these two clinical states, we developed a computational pipeline to analyze the spatial metal distribution in the LA-ICP-MS images. Our pipeline consists of three stages (Fig. 2B). First, extracting the pixels' metal values according to the pixels' intensities within the tissue segmentation mask. Second, constructing a pixel-based metal intensity histogram for each tissue section, where each value records the fraction of corresponding tissue pixels populated on that bin. Third, we used this histogram-based representation to train an Adaboost classifier that was evaluated using leave-one-patient-out cross validation. In each cross validation fold we took out one test patient's tissue samples as the testset samples. We used the pooled classification scores, obtained through all cross validation folds, to compute the ROC AUC score. We repeated this process with 100 random seeds to assess each model's stability/variation. Although our data has a slight imbalance of 40:60, 28 non responder vs 42 responder samples, it doesn't reach a severe imbalance such as 5:95 and this makes ROC AUC a reasonable metric for our case [42]. Our results revealed varying performance across different metals (Fig. 2C). Specifically, we observed marginally discriminative signals for magnesium and iron, with ROC AUC scores above the 0.5 (random classification). In contrast, copper and zinc showed ROC AUC scores close to 0.5, indicating random classification performance for these elements. These initial results highlighted that magnesium and iron may serve as potential biomarkers for patient treatment response.

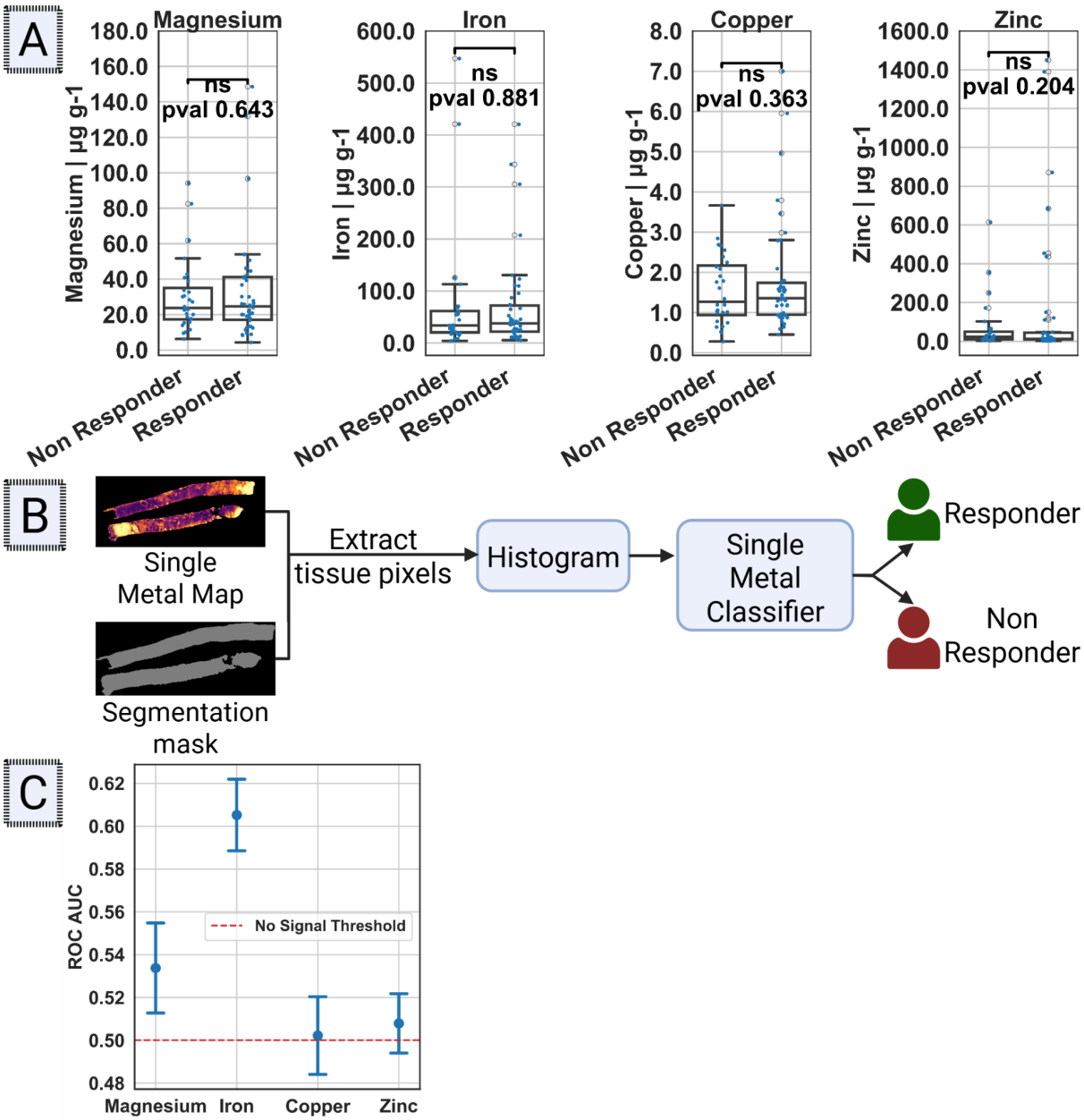

Figure 2. (**A**) Bulk measurements t-test comparison between responder and non responder tissue samples, for each metal. Bulk measurement is the average of metal readout over all pixels within the tissue segmentation mask. (**B**) Classification pipeline using single metal histogram representation of all tissue pixels within the tissue segmentation mask. (**C**) ROC AUC based on the prediction scores obtained through leaving-one-patient-out cross validation, repeated 100 times per metal.

To better understand why our metal readout distribution models did not perform well, we took a closer look at the metal distribution. We broadly identified 3 intensity intervals (Fig. 3A): (1) low pixel intensities; (2) high pixel intensities; and (3) the rest of the distribution in-between these extreme values. Spatial characterization of the low metal intensity pixels confirmed that pixels with low intensities in all metals are associated with background, i.e., holes within the tissue sample that are included in the tissue segmentation mask (Fig. 3B). Correspondingly, we defined a pixel as "background" if all of its metal intensities were below the Freedman-Diaconis estimator threshold [43], where this threshold was computed independently for each metal and each sample. Since the amount of background, non-tissue pixels, should not be associated with the disease state we excluded these pixels from the

downstream analysis. As for high metal intensity pixels - these formed a skewed distribution, with a long tail on the right - meaning a small number of high values that stretch the distribution. This property led to a sparse histogram representation where most of the pixels populate the low bins. Importantly, pixels with a high value in some, but not all, metals could be physiologically-relevant. Castellanos-Garcia et al. [44] analyzed mouse liver tissue samples and identified regions of veins characterized by high iron levels and low gold levels due to short circulation duration of positively charged nanoparticles in the bloodstream compared to negatively charged nanoparticles. Oros-Peusquens et al. [45] examined rat brain tissue sections and observed that white matter regions are characterized by high phosphorus and zinc levels but have low iron levels. In agreement with [46], [47] iron and phosphorus concentrations affect the signal transmissions in the white matter, and with [48] where zinc is related to white matter development and injury. Following these observations, we have distinguished between two populations of pixels with high intensity values and defined "outlier pixels" as pixels with high metal intensity above a percentile threshold in all metals (magnesium, iron, copper and zinc) and "hotspot pixels" as pixels with high value in at least one metal but not all. To assess the difference between these populations we examined the hotspot pixels spatial localization within the tissue and compared them to outlier pixels location. Visual comparison of hotspots spatial location over the tissue segmentation mask showed that they clustered together at coherent regions (Fig. 3C). While outlier pixels are spatially distributed as salt and pepper noise (Fig. 3C), supporting them being a technical imaging noise. In our analysis we assume that outlier pixels are caused by a technical issue and thus we exclude them from the downstream analysis.

To address the issues mentioned above, we adapted our computational pipeline as follows (Fig. 3D). First, we performed background removal by removing pixels whose all their metal intensities were below the Freedman-Diaconis estimator. Second, outlier removal was performed by removing pixels that are higher than percentile 80 across all metals. We validated that outlier with background removal did not discard too much tissue, typically removing 4% with a maximum removed fraction of 10% (Fig. S1 and Methods section). Third, as before, we constructed a pixel-based metal intensity histogram for each tissue section, where each value records the fraction of corresponding tissue pixels populated on that bin. Lastly, we used this representation to train an Adaboost classifier (Fig. 3D).

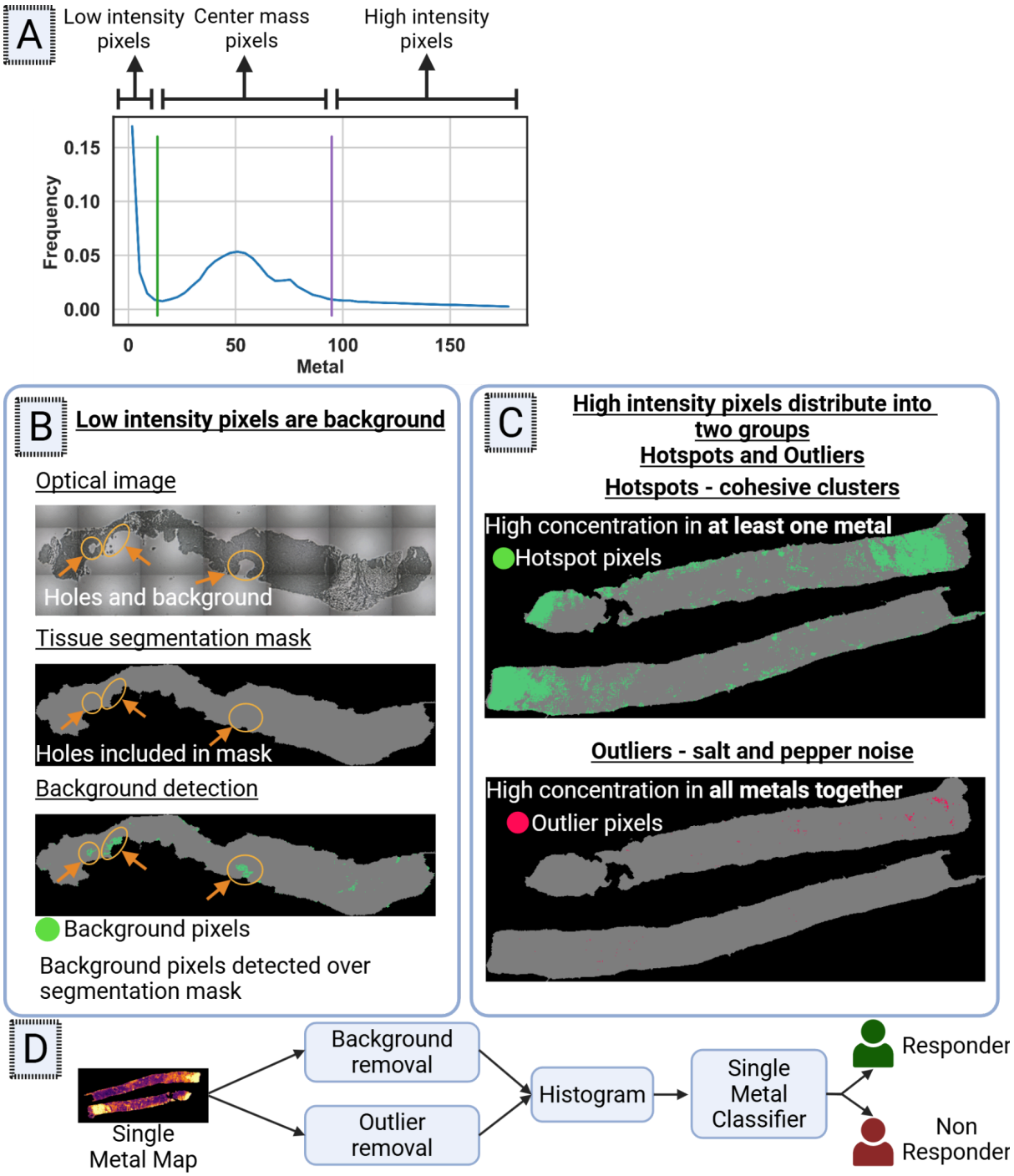

Figure 3. (**A**) Schematic drawing of typical tissue metal pixel distribution characterized by 3 pixel groups: (1) low intensity pixels, (2) distribution center mass pixels with reasonable metal intensity, (3) high intensity values which are larger by several factors than the reasonable metal intensity. (**B**) Optical image of the tissue over the sample slide with marked holes and background regions. Tissue segmentation mask, obtained during the imaging process, includes holes and background. Background pixels identified as low intensity pixels in all metals, overlaid on the tissue mask. (**C**) Spatial distribution of hotspot pixels (green) over the tissue segmentation mask (grey) compared to outlier pixels (red) spatial location produced by percentile 80 threshold. Hotspot pixels are clustered in cohesive regions compared to outlier pixels that are distributed in a salt and pepper noise manner. (**D**) Proposed classification pipeline of tissue treatment response with data preprocessing.

Hotspots are important for treatment response prediction

We assessed our proposed pipeline (Fig. 3D) using the same evaluation protocol described in previous experiments. That is using leave-one-patient-out cross validation, in each cross validation fold we took out the test patient's tissue samples as the testset samples and used their pooled classification scores, obtained through all cross validation folds, to compute the ROC AUC score. We repeated this process with 100 random seeds to assess each model's stability/variation. Our results show a weak discriminative signal ranging between AUCs of 0.66 and 0.54 for each of the metals without metal specific adjustments (Fig. 4A). We confirmed that the discrimination itself is significant by performing a permutation test, i.e. shuffling the cores' labels (Fig. S2). I will later report how we further improved the discriminative power, but before that, in the next two sub-sections, I will focus on the role of the hotspots in classification.

To verify that the hotspots were important for the prediction we took an "ablation" approach by excluding hotspot pixels from the analysis and evaluating the alteration in treatment response prediction. Specifically, we excluded all high intensity pixels according to a threshold determined for each metal separately, thus ignoring the distinction between outliers and hotspots. We evaluated thresholds determined at the 80th, 90th, 95th, and 99th percentiles of each metal. Removing all high metal values harmed the discriminative signal between different tissue states for most of the metals (Fig. 4B). These results suggest the potential role of hotspots as biomarkers for TNBC treatment response. Importantly, hotspots are determined by integrative analysis across multiple metals, thus underscoring the necessity of integrative multi metal profiling for TNBC tissue state prediction.

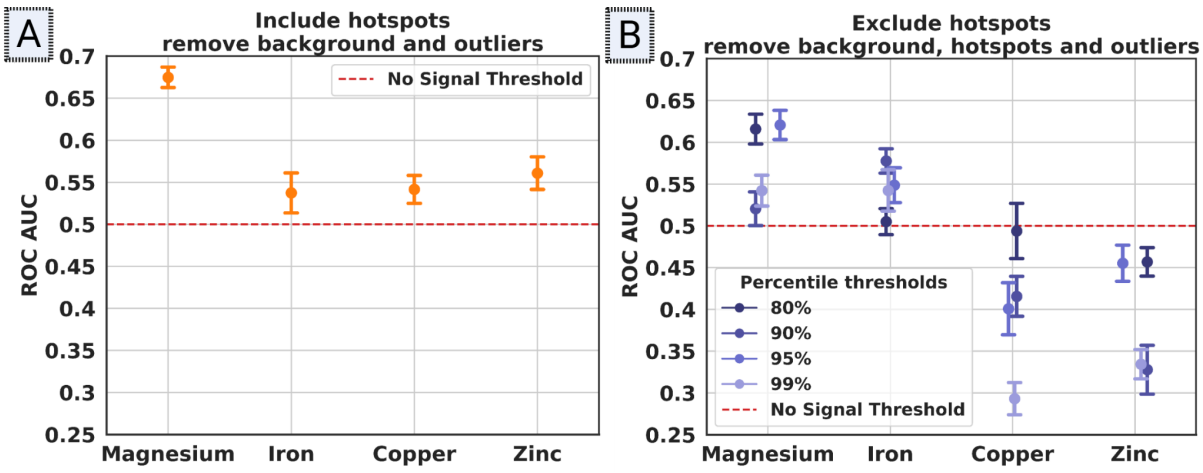

Figure 4. (**A**) ROC AUC scores of our pipeline on the preprocessed data. The tissue treatment response probability obtained through a fold of leaving one patient out cross validation, repeated 100 times per metal. (**B**) Variant of our pipeline that removes background and all high value pixels above a single metal threshold, thus removing both outliers and hotspots. ROC AUC scores are reported exactly as in Fig. 4A.

Spatial characterization of hotspots

Appreciating the potential role of hotspots in tissue disease state we next examined their spatial localization within the tissue. Hotspot pixels spatially clustered to form coherent regions of high metal composition that can not be explained by chance (Fig. 5A). Interestingly, some hotspots appeared in the context of a single metal, for example iron hotspots (Fig. 5A blue and cyan ellipse). Other hotspots emerged across multiple metal channels (e.g., yellow, red, purple, orange and pink ellipses in Fig. 5A). These repeated spatial patterns provide further support to the possibility that metal hotspots may have a physiological role in tissue disease state. To further investigate the potential biological relevance of these hotspots, we associated metal hotspots to their corresponding H&E-stained tissue sections images 12 μm apart from the tissue section used for the LA-ICP-MS acquisition (Fig. 5B). This analysis found that many of the metal hotspots resided in dense tissue regions that the pathologist decided to annotate as tumor, inflammation, and fibrous stroma (Fig. 5B, Fig. S3-S6). This association suggests that metal hotspots might have a physiological role in the context of chemotherapy resistance in TNBC tissues.

We observed that metal hotspots are concentrated in dense pathological subregions. The absence of hotspots in certain areas can be explained by the presence of sparse tissue regions, such as fat areas, which contain fewer cells compared to dense regions like tumor or inflammation. Consequently, these sparse regions exhibit much lower metallic concentrations and do not fall under the definition of hotspots. These low-concentration regions are non-informative to treatment response prediction, as demonstrated in our results when the classifier's discrimination degraded when we excluded hotspot pixels and retained the low level pixels (Fig. 4B).

It is important to note that, at this stage, this is merely a qualitative evaluation limited by the availability of detailed pathologist annotations, i.e. to 21/70 patient samples (see Fig. S7 and Methods). For each of these detailed annotated samples we counted how many pathologist annotations overlapped with hotspot clusters per metal, but did not find a clear association between specific pathologist annotations and metallic hotspots (Table S1). A comprehensive quantitative analysis will require detailed H&E annotations of more samples along with co-registration of the H&E and LA-ICP-MS images, and is left for future work.

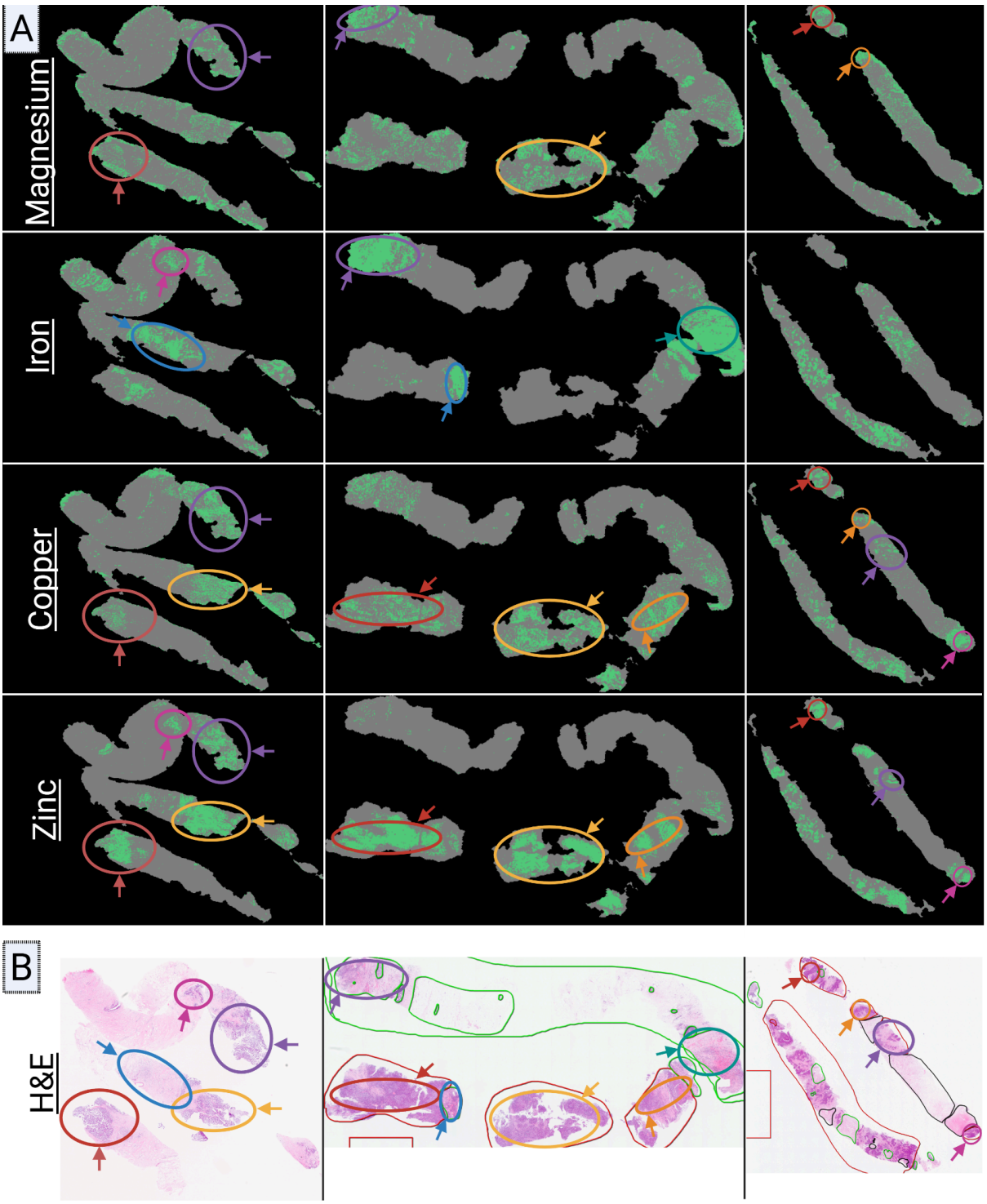

Figure 5. (**A**) Three tissue sections (columns) of samples Leap007a (left), Leap082a (center) and Leap073a (right) across 4 metals (rows). Metal's hotspot pixels (green) are overlaid over the tissue segmentation mask (grey). Hotspot regions are marked in colored ellipses and arrows in corresponding color. (**B**) Matched H&E-stained tissue sections. H&E regions that spatially associate with the hotspots are marked with the same colored ellipse and a corresponding colored arrow. Some of the hotspots overlap with pathologist annotation and dense tissue areas (fine freehand marking).

Inclusion of the magnitude encoding enhances discriminative power of metal distributions

Our machine learning evaluation relies on a normalized pixel intensity histogram-based representation and thus ignores the absolute metal magnitude. This relative representation was selected to account for the high variability, skewed, and long-tailed distributions of metal intensities across samples. A fixed-range histogram would either need an excessive number of bins to capture the full intensity spectrum or, conversely, lose crucial structural information if too few bins were used. To address this limitation, for each tissue section relative-intensity histogram representation we incorporated three additional features that encode the absolute metals' distribution (Fig. 6A-B): (1) median (2) 75th percentile, and (3) interquartile range (IQR). These features are computed directly from the tissue pixels after background and outlier removal, representing the absolute magnitude of the metallic readout in μg/g units. As shown in Fig. 6C, incorporating these magnitude encoding features improved classification performance, particularly for iron and zinc, demonstrating that absolute intensity information provides additional discriminative power. In contrast to iron and zinc, the copper classifier's performance slightly degraded with the inclusion of these absolute magnitude features. We attribute this to the observation that copper distributions across tissue samples varied more in their shape than in their overall magnitude (Fig. S8). Therefore, the magnitude-encoding features for copper exhibited low variance across the dataset, offering little discriminative power. Adding these non-informative features may have introduced noise, thereby harming the classifier's performance. These findings underscores the importance of modeling both the shape and the scale of metal distributions, rather than relying solely on normalized bin-based representations.

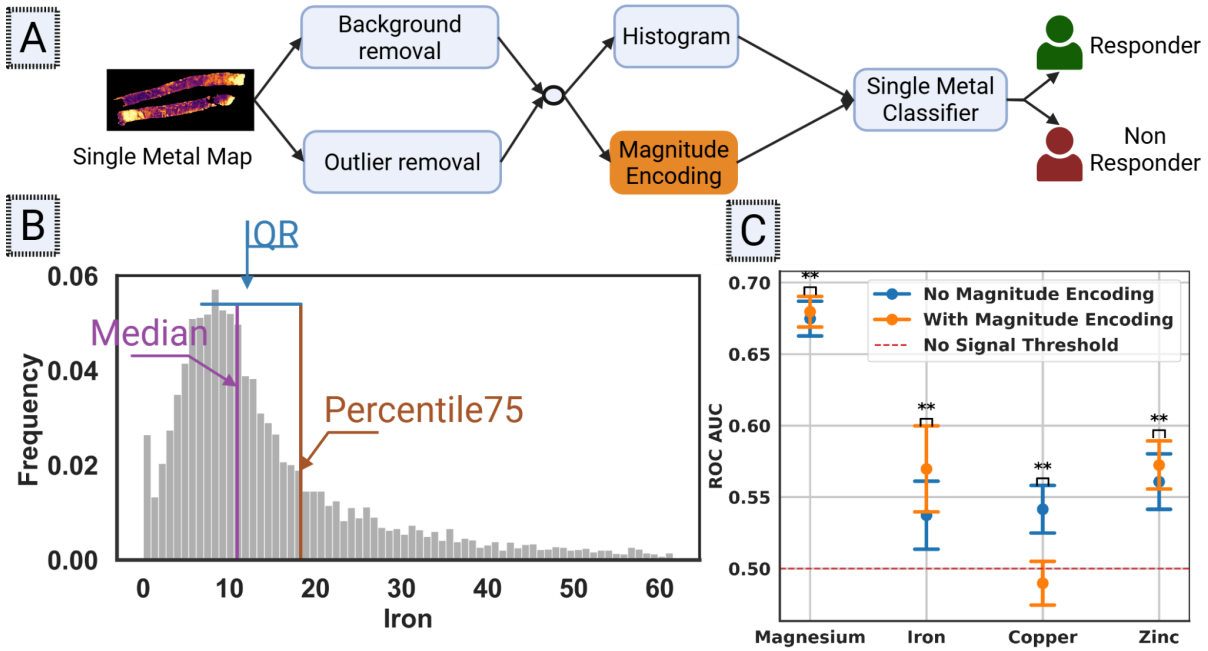

Figure 6. (**A**) Classification pipeline with the addition of magnitude encoding features to the histogram input (**B**) Schematic visualization of the median, percentile 75 and IQR of the tissue pixels (**C**) ROC AUC score comparison of the classification pipeline with and without magnitude encoding features, repeated 100 times per metal with different random seeds.

Addressing distribution skewness through data transformations

Our computational pipeline relied on histogram-based representation from raw tissue pixels after background and outlier removal. However, retaining hotspot signal results in preserving the skewed long-tailed distribution. Consequently, many bins are needed to represent the data, most of which are sparsely populated, making this representation inefficient (Fig. 7A). We therefore applied a data transformation to normalize the distribution while retaining hotspot information. A common approach is the log(x+1) transform [49], [50], which accounts for zero-valued pixels by adding a constant offset, and compresses skewed distributions. However, while log transformation mitigated skewness, it over-compressed the higher values (including hotspots) of the distribution (Fig. 7B), potentially diminishing the biological relevance of high-intensity pixels. In our work we used the Yeo-Johnson transformation [28] substantially reducing skewness by redistributing the intensity values more uniformly across the histogram bins (Fig. 7C). Yeo-Johnson transformation is designed to stabilize variance and reduce skewness, for both positive and negative values, controlled by a continuous parameter λ. Different values of λ will compress or expand different parts of the distribution, where for λ=0 Yeo-Johnson acts as the identity transformation. As Yeo and Johnson mentioned [28], an optimal λ is found using maximum likelihood estimation. To incorporate Yeo-Johnson transformation in our pipeline (Fig. 7D), we performed maximum likelihood estimation using Brent minimization [51], [52] for each sample. The transformed representation enhanced the capacity to discriminate between responders and non-responders (Fig. 7E). A permutation test, i.e., shuffling the cores' labels, confirmed that the discrimination itself is significant (Fig. 7F). These results further highlight the importance of

hotspots in treatment response classification as the transformed representation was designed to preserve these hotspots' information.

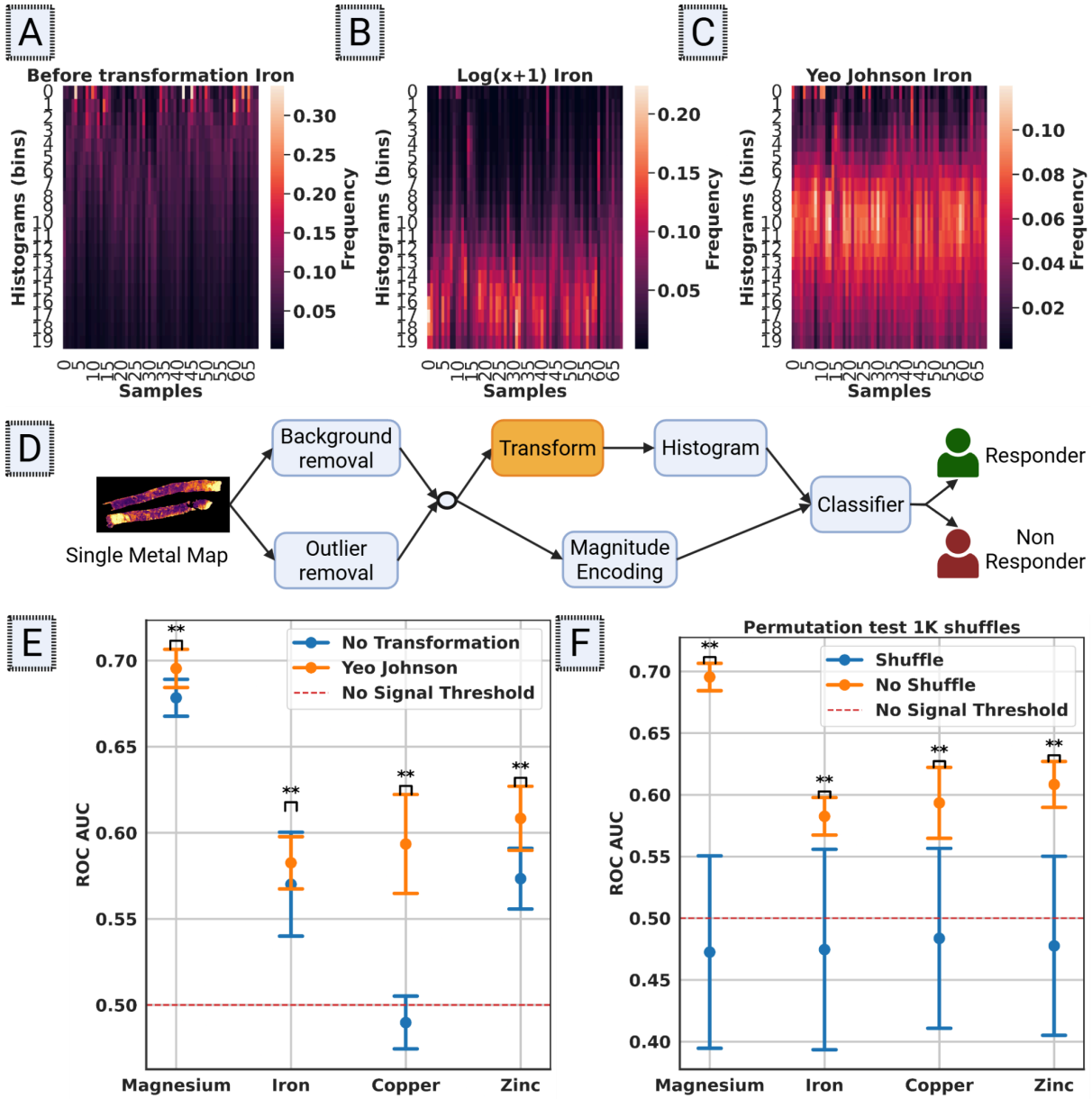

Figure 7. (**A**) Original 20-bin histogram representations (**B**) After applying log(x+1), and (**C**) After Yeo-Johnson transformation. Columns represent the cores and rows represent the histogram's bins. The intensity in a bin represents the fraction of tissue pixels populated in a specific bin, such that the integral across a core (column) sums to 1. (**D**) Revised classification pipeline. The Yeo-Johnson transformation is applied after background and outlier removal and before computing the histogram representation. (**E**) ROC AUC score comparison of the classification pipeline with and without Yeo-Johnson transform, repeated 100 times per metal with different random seeds. (**F**) Permutation test of the classification pipeline with Yeo-Johnson transform, repeated 1K times per metal with different random seeds.

Integrating multi-metal for enhanced treatment response prediction

Up to this point, our analysis focused on using the single metal distributions to classify responders versus non-responders. Where multiple metals integrative analysis contributes to hotspots identification which was shown to be considerably important to response prediction. Following this, we hypothesized that integrating predictions from multiple metal-specific models could further enhance treatment response discrimination. Rather than explicitly integrating the raw metal distributions, we have collected the prediction probabilities of the four single-metal models' (Fig. 7D) as a 4-dimensional integrative representation and computed the average of these probabilities (Fig. 8A). This integrated information improved treatment response classification to AUC of 0.76 (Fig. 8B-C), higher than the best single metal models AUC (the Magnesium) that reached 0.69. These findings suggest that multi-metal predictive modeling provides a stronger signal for treatment response classification. Although we attempted to train learning models (e.g. Logistic Regression and Adaboost) on the 4-dimensional vector of multi-metal prediction scores, they showed poorer performance compared to simple probability averaging - an outcome that may appear counterintuitive (Fig. S9).

We also experimented with training a model using the concatenated single metal representation as input, but this approach produced overfitting (Fig. S9), likely because the model couldn't learn a generalizable pattern from 92 feature input from a dataset of 70 samples. We examined how responders and non responders are separated using PCA analysis over the sample's 4-dimensional vector of metal-specific prediction probabilities. A 2D visualization of the first two PCs revealed some separation between the two groups (Fig. 8D). However, the summed explained variance ratio of the first three principal components is only 80%, suggesting that dimensionality reduction captures only part of the information. This implies that all four metal probabilities are required for responder vs non responder separation. We further analyzed which metals contribute most to the probability average classifier prediction by applying SHAP values analysis (Fig. 8E). This analysis shows that all four metals contribute to the classifier's prediction, as the SHAP values show both negative and positive contributions to the outcome.

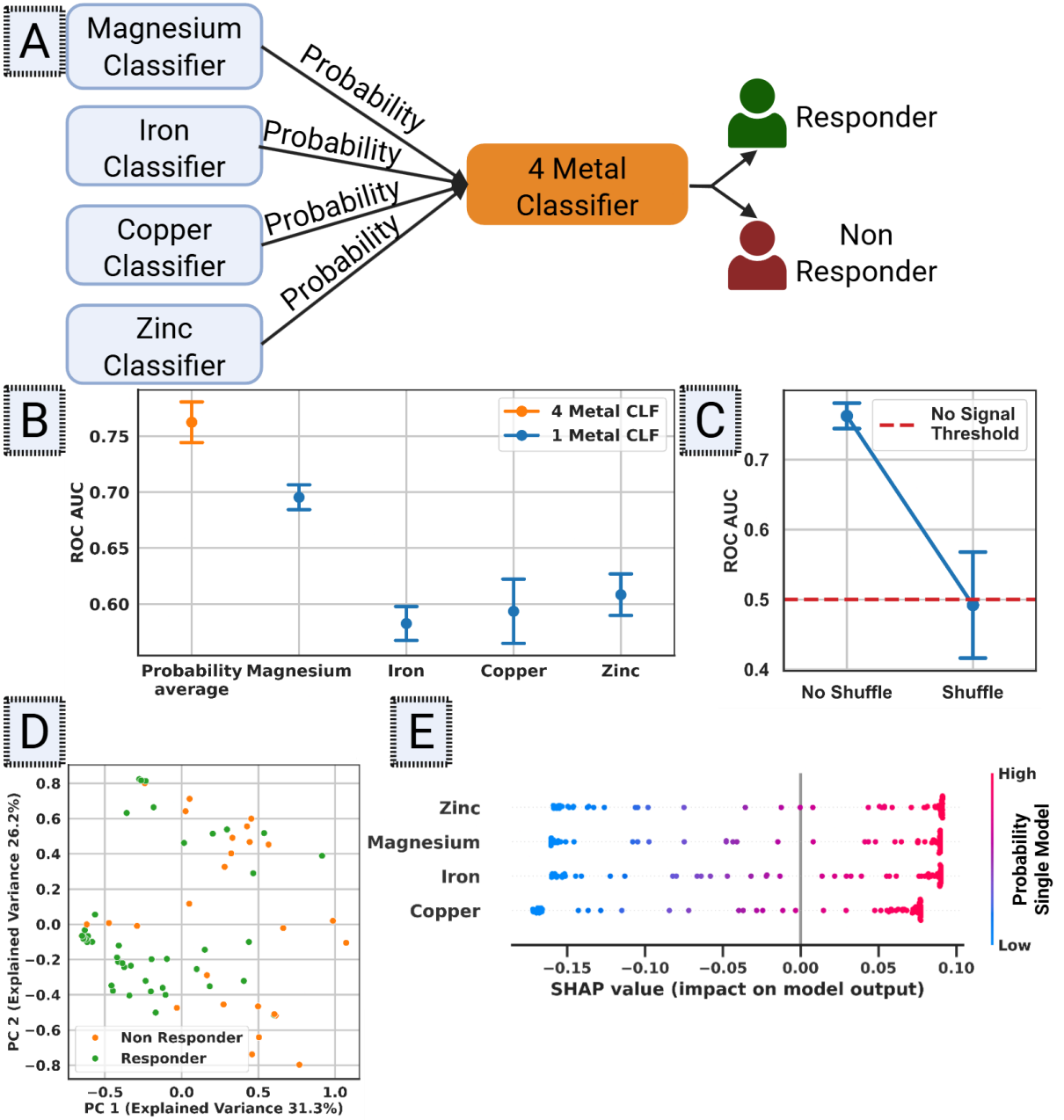

Figure 8. (**A**) Classification pipeline that relies on the sample's treatment response probability of all 4 single metal models. (**B**) ROC AUC score of averaging four single-metal models' output probabilities (orange) vs single metal classification pipeline (Fig 4A) applied per metal. The experiment was repeated 100 times per metal with different random seeds for the single metal classification pipeline. The probability average was tested on the results of these 100 repetitions due to its determinism. (**C**) Permutation test of the four metal classification pipeline (averaging probabilities), repeated 1K times with different random seeds. (**D**) 2D PCA analysis examining the separation between responders vs non responders. Each sample is represented by a 4D probability vector, with scores derived from the four single metal models. These probabilities were taken from one of the 100 runs performed in Fig. 8B. (**E**) SHAP values analysis of averaging four single-metal models' output probabilities taken from one of the 100 runs performed in Fig. 8B. X axis represents the SHAP value for each single metal model probability. Each dot represents a sample and its color represents the probability of a single metal model.

Discussion

Our study introduces a computational pipeline for the quantitative spatial analysis of multi metal imaging data. For the first time, we provide a systematic analysis of LA-ICP-MS imaging and demonstrate the spatial relationships in and between metals in neoadjuvant chemotherapy (NACT) response prediction. We showed that each of the metals, magnesium, iron, copper, and zinc, hold a predictive signal for NACT response in TNBC. Our results demonstrated a predictive signal using a single-metal model, as well as using 4D integrative representation of the 4 single models' probabilities. In multi metal integration the predictive signal increased and each metal contributed to the final prediction. Contrary to previous LA-ICP-MS studies that rely on expert-annotated regions or semi-quantitative comparisons [23], [24], [25], [26], our approach discovered predictive patterns that were not pre-defined by a human annotator. A central finding is the identification of "hotspot pixels" - high value pixels in at least one metal but not all. We found that these hotspots are not random artifacts and that they are spatially clustered to form coherent regions of high metal composition. Furthermore, the repeated occurrence of these hotspots across multiple metal channels in areas that coincide with pathologist annotations supports the likelihood of a physiological role in the tissue's disease state.

Our findings support and extend the existing literature that links magnesium, zinc, and copper to TNBC and breast cancer. It's known that in breast cancer malignant cells often upregulate magnesium transport channels to increase intracellular magnesium levels, which fuels tumor cell growth through its function of increased energy demand [17]. Cancer patients often exhibit high copper levels in both tumor tissue and serum, reflecting tumor cells' increased demand for this element [53]. Additionally other studies showed that breast cancer patients with poor prognosis exhibit higher levels of copper importers and copper binding protein [54], [55], [56]. Breast tumor tissues have been found to contain significantly higher zinc concentrations than normal breast epithelium [57], [58], [59], with the most elevated zinc levels reported in TNBC [25]. Malignant cells achieve this in part by overexpressing zinc importers to boost zinc uptake. Notably, increased expression of zinc transporters correlates with higher tumor grade and severity [59]. Our spatial analysis of hotspot regions with pathologist annotations coincide with these results, showing that hotspots for these three metals are typically located within pathologist-annotated tumor regions (Table S1). In addition, our work reveals a new dimension - we found that these metal-rich regions have a predictive signal for NACT response. This suggests that within the tumor mass, tumor subregions characterized by high metal accumulation may point to a cellular state that is resistant to chemotherapy.

Despite these promising findings, there are several limitations to our study that should be addressed in future work. First, although our cohort of 70 samples is larger than many previous LA-ICP-MS studies, it is still relatively small for training machine learning based models. Despite this, we could still extract biological insights using simple representations. Second, while our analysis suggests that hotspots correspond to histologically dense regions,

the correlation between high-intensity metal regions and histological features still requires more systematic investigation.

Methods

TNBC Patient dataset

In this study, we used the TNBC patients tissue samples cohort collected by our collaborators from Maddy Parsons's team in King's College London as part of the Δ-Tissue project. This Single-Arm Prospective cohort includes 94 core biopsy tissue samples from 89 TNBC patients, collected before or during neoadjuvant chemotherapy (NACT). Of these, 80 samples (from 75 patients) were collected prior to treatment, and 14 samples (from 8 patients) were collected during treatment. The difference between the number of patients and the number of samples reflects cases where large biopsy samples were split and imaged separately. Pretreatment samples were preserved in Formalin-Fixed Paraffin-Embedded (FFPE) blocks and the 14 samples collected during treatment were snap-frozen. After chemotherapy, each patient was assigned a Residual Cancer Burden (RCB) score and labeled as either a "responder" or a "non-responder" (Fig. 1A). Non-responders who died within two years were further labeled as "extreme non-responders". Due to inaccurate lab evaluations, only 70 of the 80 pretreatment samples (from 66 patients) had reliable response labels. The dataset also includes resection tissue samples from patients who did not respond to chemotherapy and therefore underwent surgery. We also note that, in this dataset, no metadata is available for any of the patients. In this work, we focus on predicting treatment response (responder vs non-responder), using 70 pretreatment samples (from 66 patients) with reliable labels, this resulted in an imbalanced dataset, both at the patient level and at the sample level (Fig. 1B).

Each tissue sample in the dataset was sectioned into six matched slices, 4 μm apart. Each slice was imaged by our collaborators from Maddy Parson's team using a different technique: Hematoxylin and Eosin (H&E) staining, Spatial Transcriptomics (ST), Imaging Mass Cytometry (IMC), Laser Ablation Inductively Coupled Plasma Mass Spectrometry (LA-ICP-MS), Fluorescence Lifetime Imaging Microscopy (FLIM), and Desorption Electrospray Ionization (DESI). In this work, we analyzed two matched tissue sections collected 12 μm apart, for each sample. One section was imaged by H&E staining and then annotated by a pathologist from Maddy's team. Detailed pathologist annotations were available for 21 out of 70 tissue samples (e.g. Fig. S7), marking pathological entities such as invasive tumor, fibrous tissue, tumor with inflammation, and others. The other matched tissue section, used in our analysis, was imaged by LA-ICP-MS for magnesium, iron, copper and zinc (Fig. 1C). Our primary analysis focused on using LA-ICP-MS images of spatial metal distribution to predict treatment response. We then visually compared the metal maps to pathological annotations of the H&E images from the matched tissue section.

LA-ICP-MS imaging captures the spatial distribution of metal ions by measuring their intensities at specific mass-to-charge ratios (m/z) over time, generating time series data of the

measured mass, the laser's spatial location and the time of sample ablation. Due to the long imaging duration per sample, the dataset was imaged in batches, each containing 3-4 samples imaged on the same day. To mitigate batch effects, our collaborator Dr. Alex Morrell from Maddy's team calibrated the intensity readout using certified reference materials (CRM). CRM measurements were performed twice, during each batch: once before imaging the first sample and once after the last sample of the day. The LA-ICP-MS time-series data were reconstructed into two-dimensional (2D) images, with separate channels representing specific metals: magnesium, manganese, iron, copper and zinc. Each pixel in these metal maps corresponds to a metal concentration readout in μg/g units, at a spatial resolution of 20 μm per pixel. Approximately 50% of the samples had corrupted manganese readouts because imaging began during the machine's initialization phase. While calibration successfully recovered magnesium, iron, copper and zinc readouts, manganese measurements remained unreliable. Therefore, manganese was excluded from further analysis. To reduce imaging time, Dr. Alex Morrell predefined key points for laser ablation that marked the start and end positions of each tissue sample within the field of view of the imaging machine. This approach simplified the manual thresholding of background versus tissue signal in the raw time series data. Using this manual thresholding combined with the reconstructed 2D LA-ICP-MS image, a segmentation mask was created to distinguish tissue from background (Fig. 1C). However, this segmentation mask did not account for holes within the tissue resulting in a high pixel count at lower intensity values (Fig. 3B).

Computational analysis pipeline

We developed a computational pipeline to predict NACT response from LA-ICP-MS images. For each metal channel (magnesium, iron, copper, and zinc), we trained a separate predictive model. While each model was trained independently, it leveraged information from all four metals to distinguish hotspot regions from outliers. Finally, we integrated the predictions from the four single-metal models into an improved final classification.

Image Preprocessing and Hotspot Identification

Our initial attempts to predict treatment response based on the raw tissue pixels were limited (Fig. 2). A closer examination of the metal distributions, we identified 3 intensity intervals (Fig. 3A) background, hotspots and outliers. This led to a multi-metal preprocessing step applied within the tissue segmentation mask. Our main goal was to establish a pipeline that identifies discriminative signals across all metals using consistent parameters without metal-specific optimizations, because otherwise our pipeline might capture discriminative signals that were found by chance due to complex metal specific data processing.

Background Removal: Pixels were defined as *background* if their intensity fell below a threshold determined by the Freedman-Diaconis estimator, applied independently to each metal channel within each tissue sample. This estimator is commonly used to determine optimal bin width for histograms and defined as: $bin\,width = 2 \cdot \frac{IQR}{\sqrt[3]{n}}$, with the width being proportional to the interquartile range (IQR) of the pixel intensities (a measure of

spread), and inversely proportional to the cube root of n, the number of pixels within the tissue segmentation mask for that sample. This formula balances two factors: the spread of the data (capturing variability) and the number of observations (ensuring statistical stability). A narrower bin width is chosen when more data points are available, allowing finer resolution, while a wider bin is used when data is sparse to avoid overfitting noise. We chose the Freedman-Diaconis method because of its robustness to high value pixels, and its ability to adapt the threshold dynamically across samples and channels. Visual inspection of the first bin removed for each histogram (Fig. 3B) confirmed that pixels with low intensities across all metals were typically located in background regions, such as holes within the tissue that were included in the tissue segmentation mask (Fig. 3B).

Outlier Removal: Pixels with intensities above the 80th percentile in all four metals (magnesium, iron, copper and zinc) were defined as *outliers*. These pixels were removed from the analysis, as they likely represent imaging artifacts, such as salt-and-pepper noise. The 80 percentile threshold was chosen empirically to balance the exclusion of extreme values with the preservation of relevant tissue data, typically removing less than 4% of tissue pixels per sample, with a maximum of 10% (Fig. S1). We verified that identifying outliers based on all four metals is essential, while removing pixels that are extreme in only one metal would also eliminate hotspot regions, which were shown to be important for accurate response classification (Fig. 4).

Single-metal feature representation

For each preprocessed metal map, we constructed a feature vector for every tissue sample. This process was designed to capture the shape of the metal's spatial distribution while mitigating issues of data skewness, and varying intensity ranges across samples. After background and outlier pixels removal the tissue pixels are used to produce magnitude encoded features, separately these tissue pixels underwent Yeo-Johnson transformation and the transformed values were used for creating the histogram representation.

Yeo-Johnson Transformation: After background and outlier pixels removal, the raw intensity values of the remaining pixels for each sample were transformed using the Yeo-Johnson transformation [28]. This step was critical for reducing the severe skewness that presents in the metal intensity distributions. This transformation creates a more balanced distribution without over-compressing the high-intensity hotspot values, a known limitation of log-transformations (Fig. 7). Yeo-Johnson transformation is designed to stabilize variance and reduce skewness controlled by a continuous parameter λ. Different values of λ will compress or expand different parts of the distribution, including when $\lambda=0$ Yeo-Johnson acts as the identity transformation. As Yeo and Johnson mentioned [28], an optimal λ is found using maximum likelihood estimation, in this work optimal λ was found for each metal tissue pixel and for each sample using maximum likelihood estimation using Brent minimization [51], [52]. Brent's method [52] is a numerical optimization algorithm used to find the local minimum of a single-variable function within a given interval without requiring its derivative and guarantees convergence. This method is useful due to the speed of quadratic approximation and the guaranteed convergence of the bracketing method.

Histogram representation: The transformed tissue pixel intensities were then binned into a 20-bin histogram. The frequency of tissue pixels in each bin was normalized to create a 20-dimensional feature vector representing the shape of the metal's distribution for that sample. The bin count was determined to be 20 after comparing histograms constructed with 10, 20, and 30 bins (Fig. S10). This choice is based on a balance between resolution and feature space dimensionality. A 10-bin histogram was found to be too coarse, obscuring important details of the intensity distribution. Conversely, a 30-bin histogram resulted in a sparse and inefficient representation, unnecessarily increasing the number of features for a dataset of our size, which could increase the risk of model overfitting.

Magnitude encoding: Since the sample's histogram is a normalized metal intensity representation, it loses information about the absolute magnitude of the metal. This relative representation was selected to account for the high variability, skewed, and long-tailed distributions of metal intensities across samples. An alternative fixed-range histogram would either need an excessive number of bins to capture the full intensity spectrum or, conversely, lose crucial structural information if too few bins are used. Thus, we added three additional features that encode the absolute metals' distribution: (1) median, (2) 75th percentile, and (3) interquartile range (IQR) from the sample's absolute tissue pixel intensities. These magnitude encoding features, appended to the histogram feature vector, are measured after preprocessing and before transformation.

Model Training and Evaluation

We trained a predictive single-metal model for each of the four metals using the metal's feature vector described above and used the same model parameters, training and evaluation protocol for the experiments described in the results sections 4.1-4.5. We used an AdaBoost classifier consisting of an ensemble of 50 decision trees, maximum depth 3 and minimum sample split 8. We set class weights to be inversely proportional to their frequencies for handling the response class imbalance - 42 responder samples and 28 non responder samples. Model performance was evaluated using a leave-one-patient-out cross-validation (LOOCV) strategy. In each fold, all samples from a single patient were held out as the test set, ensuring that predictions for a patient were made by a model that had not been trained on any of their tissue samples. The performance was measured by the ROC AUC score, which was computed by aggregating the predicted responder probabilities from test set samples in each fold of all LOOCV folds. The ROC AUC score was measured on the samples and not on the patients, because in our analysis we had 4/66 patients with a pretreatment sample that was divided into two chunks and these two chunks were imaged separately. The decision of measuring the ROC AUC per sample was due to minor influence of these 4/70 (only 5%) extra samples from the same patients. Additionally, these two samples from the same patient were imaged separately introducing potential batch effect differences of metallic readout. To ensure the robustness of our results, the entire training and evaluation process was repeated 100 times with different random seeds.

Multi-Metal Prediction Integration

We integrated the responder probability outputs from the individual single-metal models, constructing a 4D representation of probabilities. We tested several models that used this representation for treatment response prediction: (1) averaging probabilities, (2) Logistic Regression and (3) Adaboost. When we used the same hyperparameters for Adaboost, i.e. 50 decision trees, maximum depth 3 and minimum sample split 8. Additionally, class weights were set to be inversely proportional to their frequencies for handling the response class imbalance (42 responder samples and 28 non responder samples). Logistic Regression and Adaboost were trained on random seed results of a single-metal model predicted probability results. Logistic Regression and Adaboost performance was evaluated using LOOCV and the ROC AUC score was computed by aggregating the predicted responder probabilities from test set samples in each fold of all LOOCV folds. This evaluation was repeated 100 times with different random seeds. Due to absence of training and the determinism of averaging probabilities, the prediction results of 100 repetitions of single-metal models LOOCV were used to measure the stability of this method. Averaging probabilities approach significantly improved classification performance compared to any single-metal models alone, demonstrating that multi-metal predictive modeling provides a more enhanced signal for treatment response classification (Fig. 8B). We further conducted a permutation test for averaging, to test the stability of this method results, by shuffling the ground truth labels 1K times and measuring the ROC AUC for each shuffle (Fig. 8C). Although we attempted to train Logistic Regression and Adaboost, they both showed poorer results compared to averaging probabilities (Fig. S9). We also experimented to train an Adaboost model with the same hyperparameters on concatenated feature vector representation from each metal. But this approach produced overfitting (Fig. S9), likely because the model couldn't learn a generalizable pattern from 92 feature input from a dataset of 70 samples.

Metal importance for 4 metal integrative representation

To examine the metal importance for responder vs non responder classification we made PCA analysis and SHAP analysis. We examined how responders and non responders are separated using 2D PCA analysis over the sample's 4D probability representation (Fig. 8D). We used PCA analysis of 4D probability representations from one of the 100 repetitions of all single-metal classifiers LOOCV. Based on the separation and PCA explained variance ratio of the first 3 PCA components, they can explain only 80% of the data. Meaning that there isn't an inferior metal that is redundant compared to the other metals. Then we used SHAP values analysis which metals mostly affect the probability average classifier (Fig. 8E). Similarly as for PCA analysis, we used one of the 100 repetitions of all single-metal classifiers LOOCV.

Hotspot spatial comparison to H&E pathologist annotations

For visual comparison of hotspots per metal to pathologist annotations, we plotted the hotspot over the tissue mask and compared to pathologist annotations on similar places. If the hotspot cluster was large enough to significantly and clearly overlap with the annotation then we marked it (Fig. 5 and Fig. S3-S6) and counted this annotation as overlapped with hotspots in

Table S1. So for each sample and each metal we counted how many annotations for each type had a significant overlap with hotspot regions, e.g. tumor, inflammation (inflam) and fibrous stroma. We observed hotspot clusters in all LA-ICP-MS images, however we could examine them to pathologist annotations only in 21/70 tissue samples. Because we have detailed pathologist annotations only for these samples (Fig. S7).

Supplementary Figures

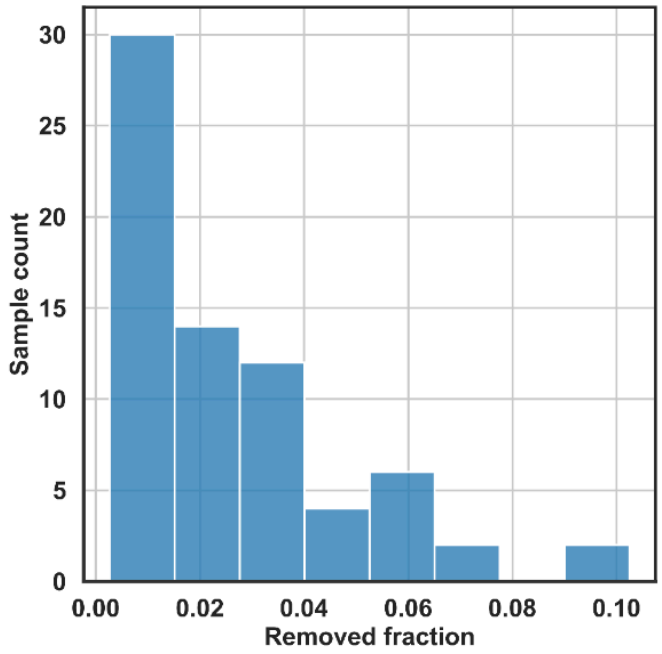

Figure S1. Histogram of samples count showing the fraction of pixels removed at each sample due to background and outlier removal.

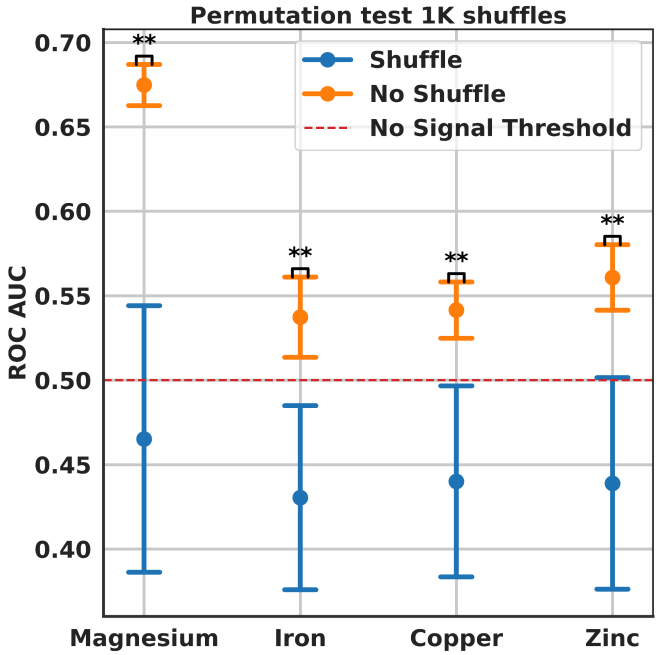

Figure S2. Permutation test of the classification pipeline with background and outlier removal (Fig. 3D), repeated 1K times per metal with different random seeds.

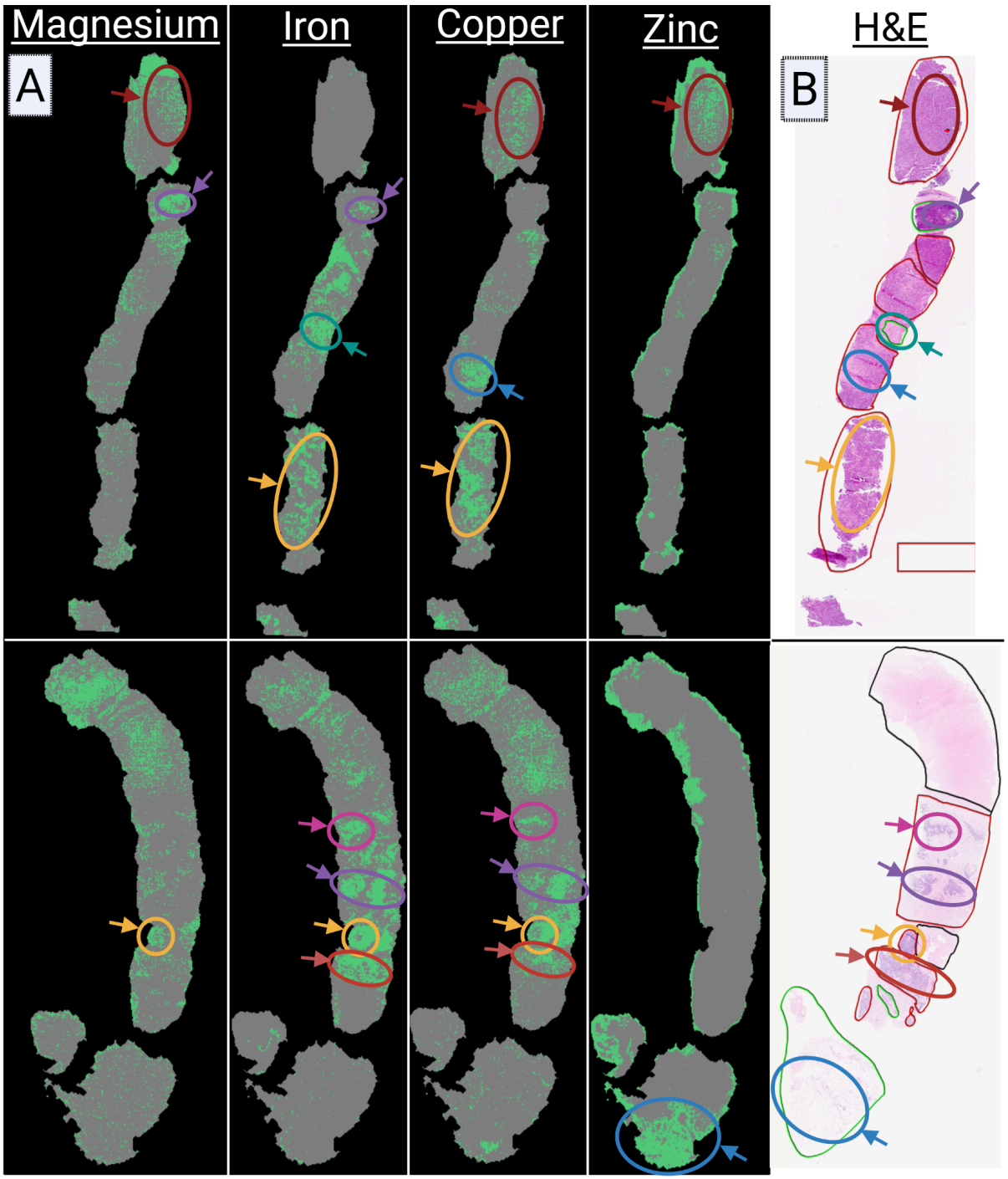

Figure S3. (**A**) Two tissue sections (rows) of samples Leap013a (top) and Leap032a (bottom) across 4 metals (columns) and matched pathologist annotated H&E image of the tissue section. For each tissue section metal's hotspot pixels (green) are overlaid over the tissue segmentation mask (grey). Hotspot regions are marked in colored ellipses and arrows in corresponding color. (**B**) H&E-stained tissue sections images 12 µm apart from the tissue section used in Fig. S3A. H&E regions that spatially associate with the hotspots are marked with a colored ellipse and a corresponding colored arrow. Some of the hotspots overlap with pathologist annotation and dense tissue areas.

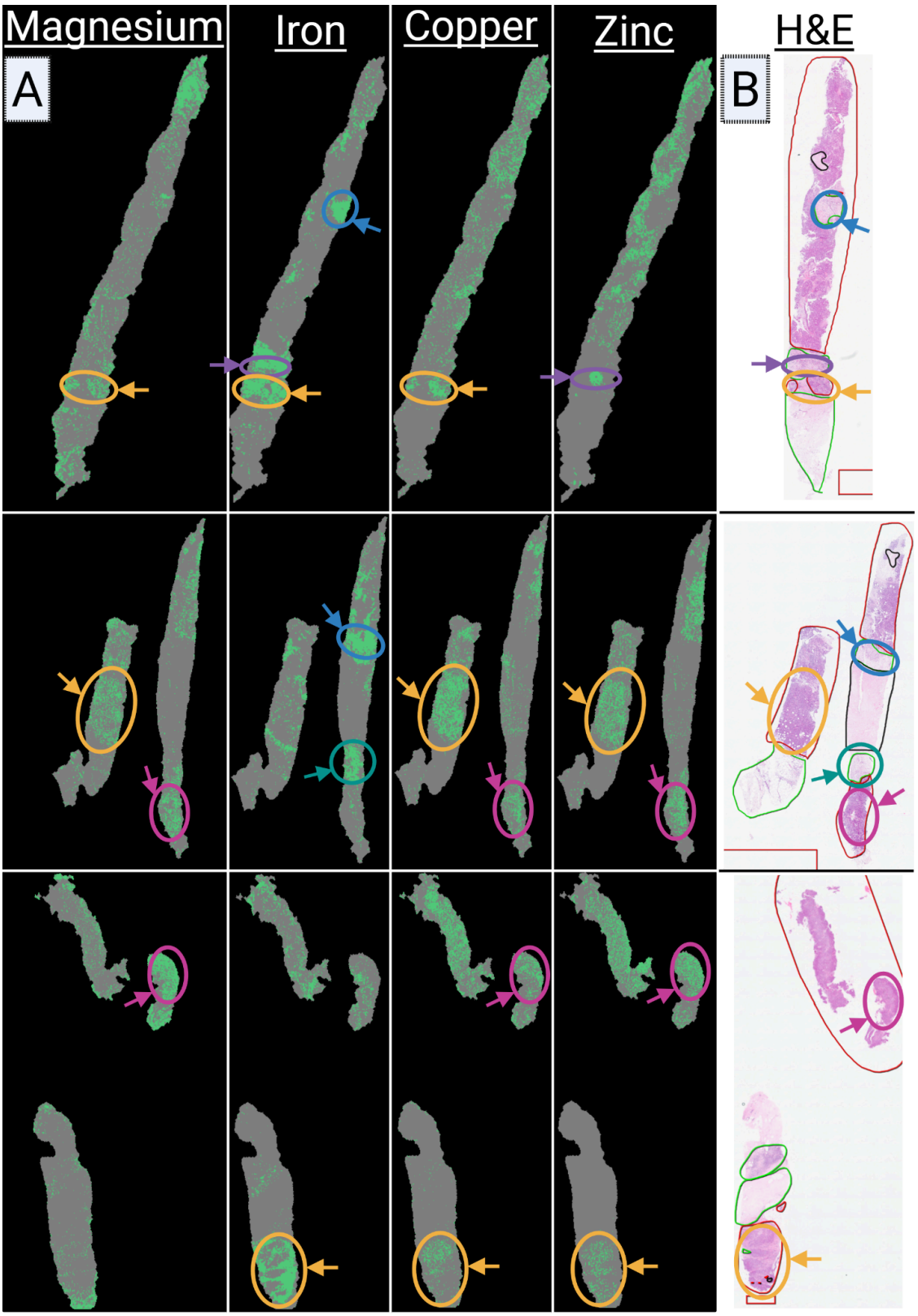

Figure S4. (**A**) Three tissue sections (rows) of samples Leap080a (top), Leap069a (center) and Leap068a (bottom) across 4 metals (columns) and matched pathologist annotated H&E image of the tissue section. For each tissue section metal's hotspot pixels (green) are overlaid over the tissue segmentation mask (grey). Hotspot regions are marked in colored ellipses and arrows in corresponding color. (**B**) H&E-stained tissue sections images 12 µm apart from the tissue section used in Fig. S4A. H&E regions that spatially associate with the hotspots are marked with a colored ellipse and a corresponding colored arrow. Some of the hotspots overlap with pathologist annotation and dense tissue areas.

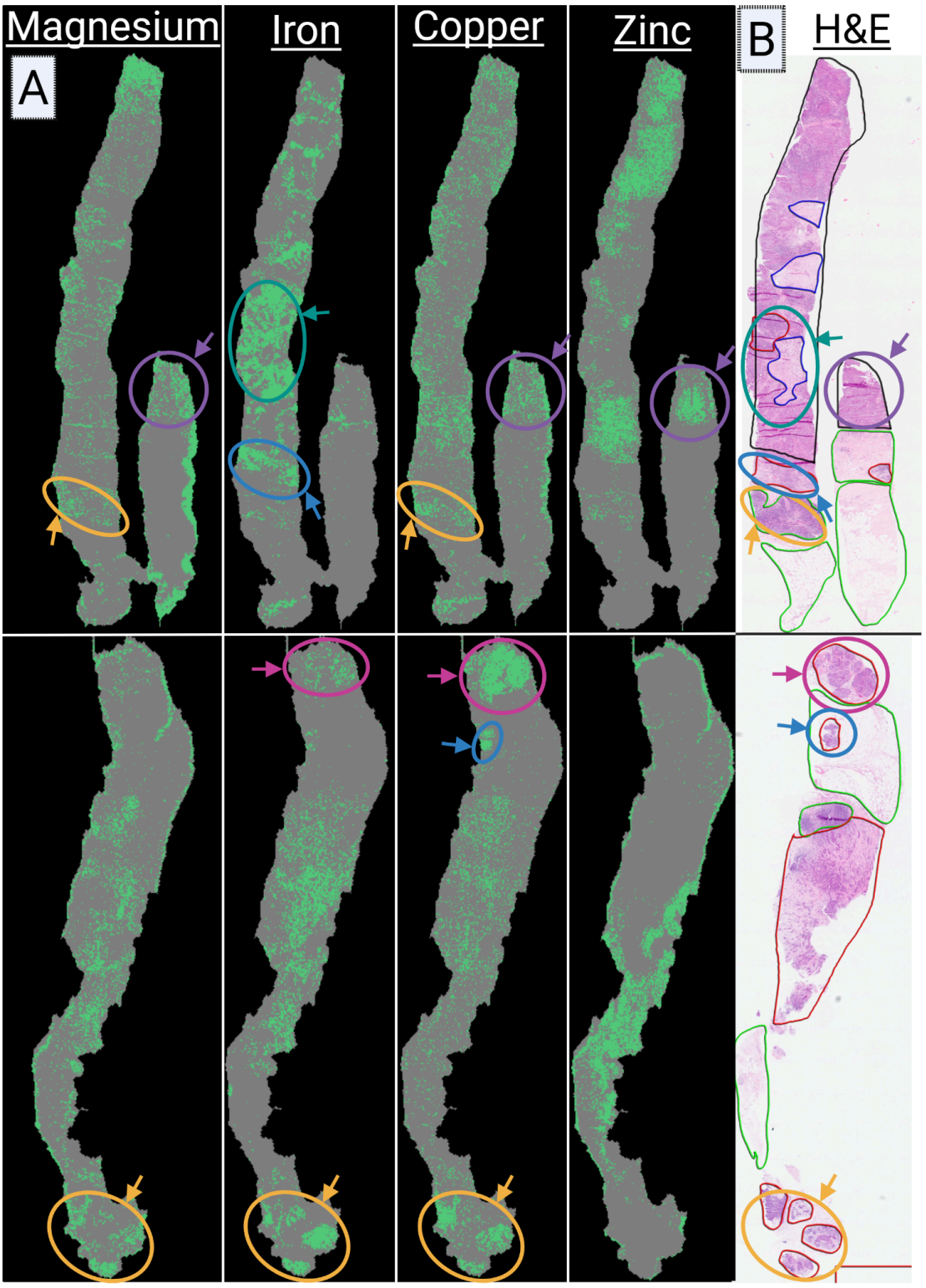

Figure S5. (**A**) Two tissue sections (rows) of samples Leap105a (top) and Leap090a (bottom) across 4 metals (columns) and matched pathologist annotated H&E image of the tissue section. For each tissue section metal's hotspot pixels (green) are overlaid over the tissue segmentation mask (grey). Hotspot regions are marked in colored ellipses and arrows in corresponding color. (**B**) H&E-stained tissue sections images 12 µm apart from the tissue section used in Fig. S5A. H&E regions that spatially associate with the hotspots are marked with a colored ellipse and a corresponding colored arrow. Some of the hotspots overlap with pathologist annotation and dense tissue areas.

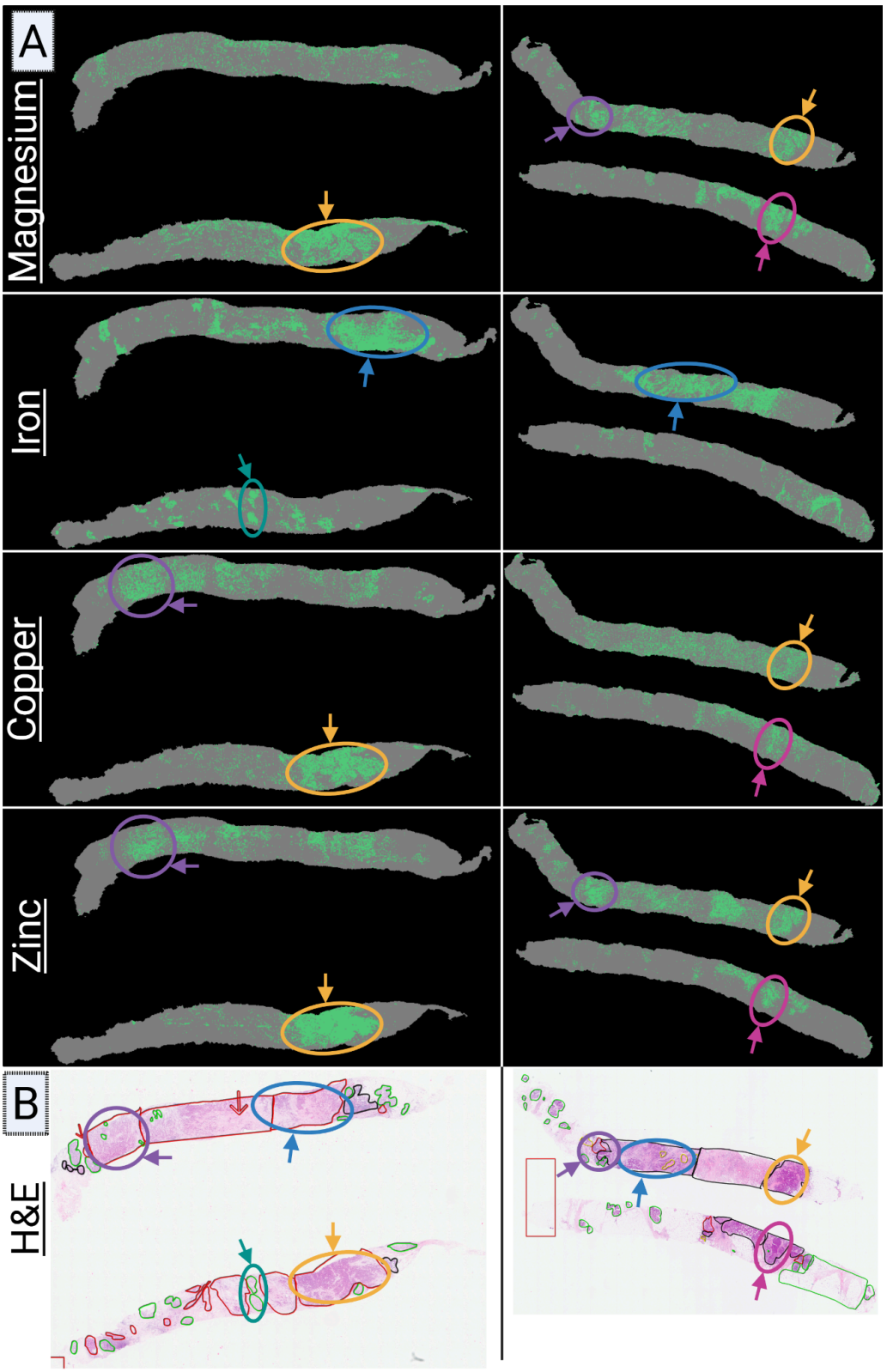

Figure S6. (**A**) Two tissue sections (rows) of samples Leap106a (left) and Leap087a (right) across 4 metals (columns) and matched pathologist annotated H&E image of the tissue section. For each tissue section metal's hotspot pixels (green) are overlaid over the tissue segmentation mask (grey). Hotspot regions are marked in colored ellipses and arrows in corresponding color. (**B**) H&E-stained tissue sections images 12 µm apart from the tissue section used in Fig. S6A. H&E regions that spatially associate with the hotspots are marked with a colored ellipse and a corresponding colored arrow. Some of the hotspots overlap with pathologist annotation and dense tissue areas.

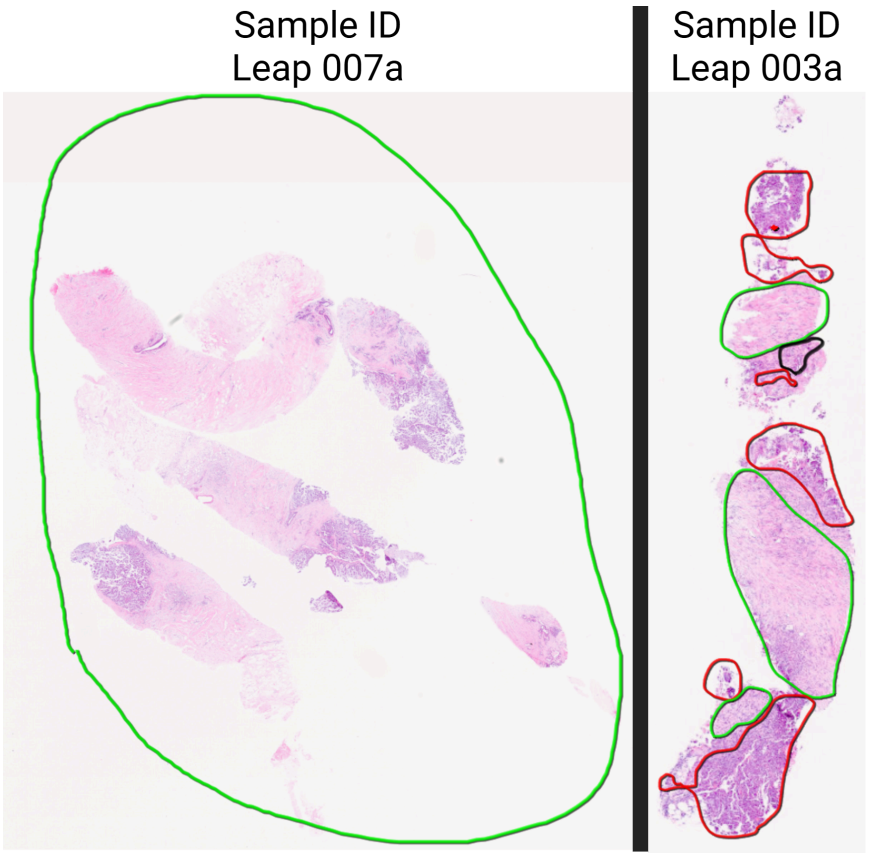

Figure S7. (Left) Tissue sample with non granular expert annotation (Right) Tissue sample with granular expert annotation. In the left example the annotation marks the whole tissue sample without addressing the local subregions unlike the right example: e.g. tumor area, normal tissue, fibrous stroma etc.

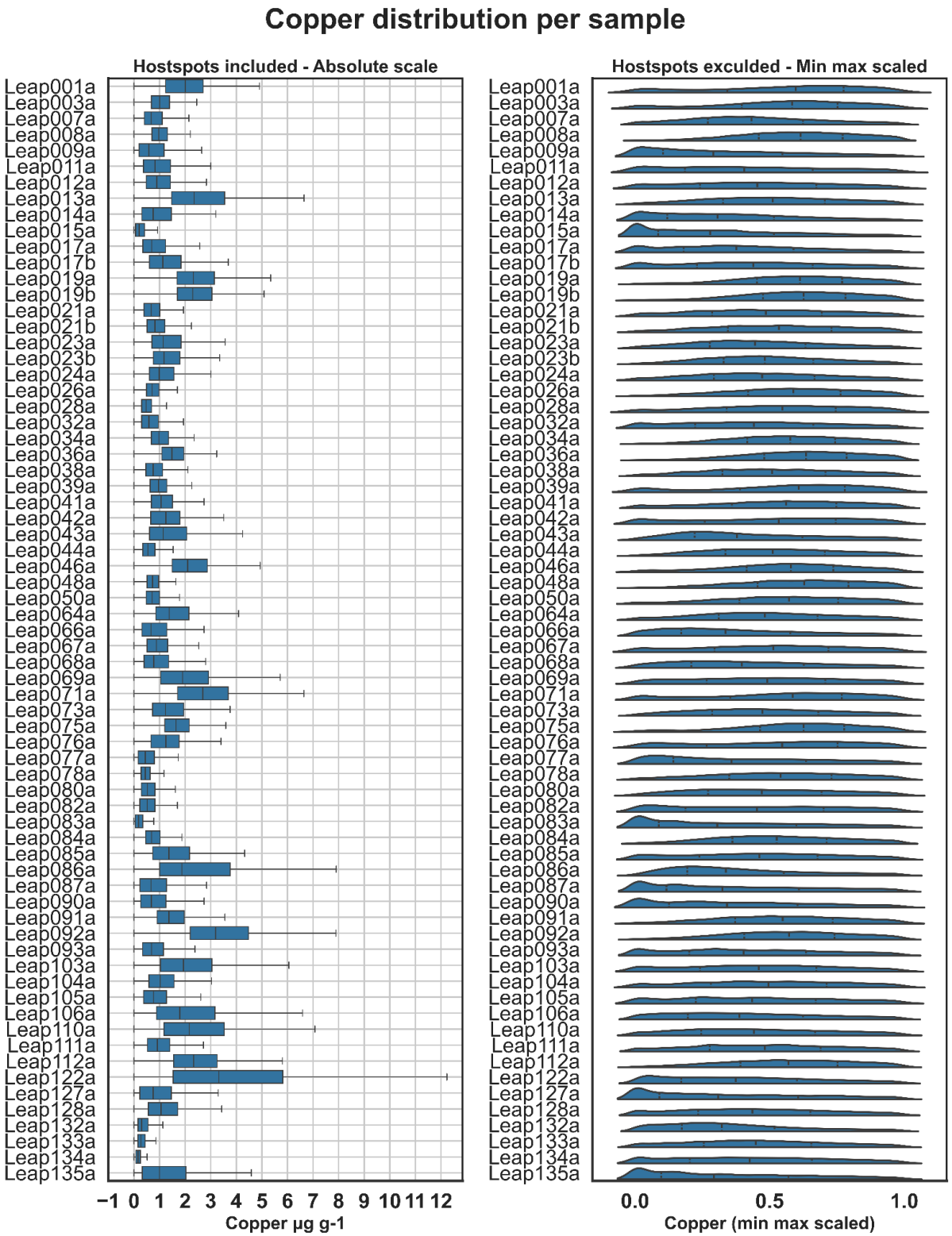

Figure S8. Copper readout distribution per sample when hotspots are included. (Left) shows the boxplot of the distribution in absolute scale. (Right) shows the distribution shape in min max scaled per sample, hotspots are excluded for better visualization otherwise they will add a very long right tail. As we can see the magnitude encoding features (median, quantile 75 and IQR) vary less for most of the samples compared to the distribution shape on the right figure.

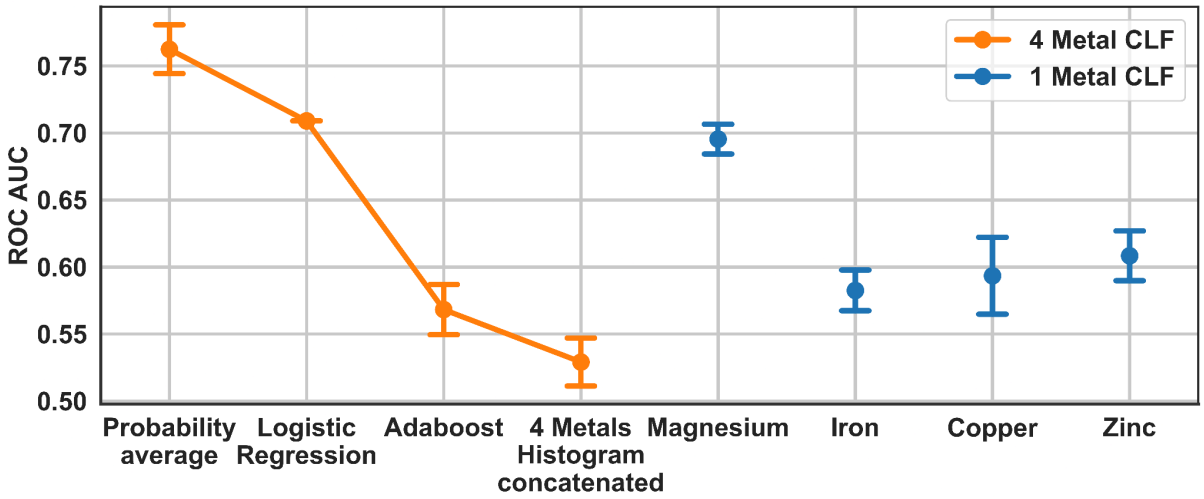

Figure S9. ROC AUC score of 4 metals model (orange) that takes as an input four single-metal models' output probabilities and (left to right) apply averaging, train Logistic Regression, Adaboost or Adaboost trained on concatenated 4 metals sample representation of Fig. 7D and compared to (blue) single metal classification pipeline (Fig 4A) applied per metal. The experiment was repeated 100 times per metal with different random seeds for the single metal classification pipeline. The probability average was tested on the results of these 100 repetitions due to its determinism.

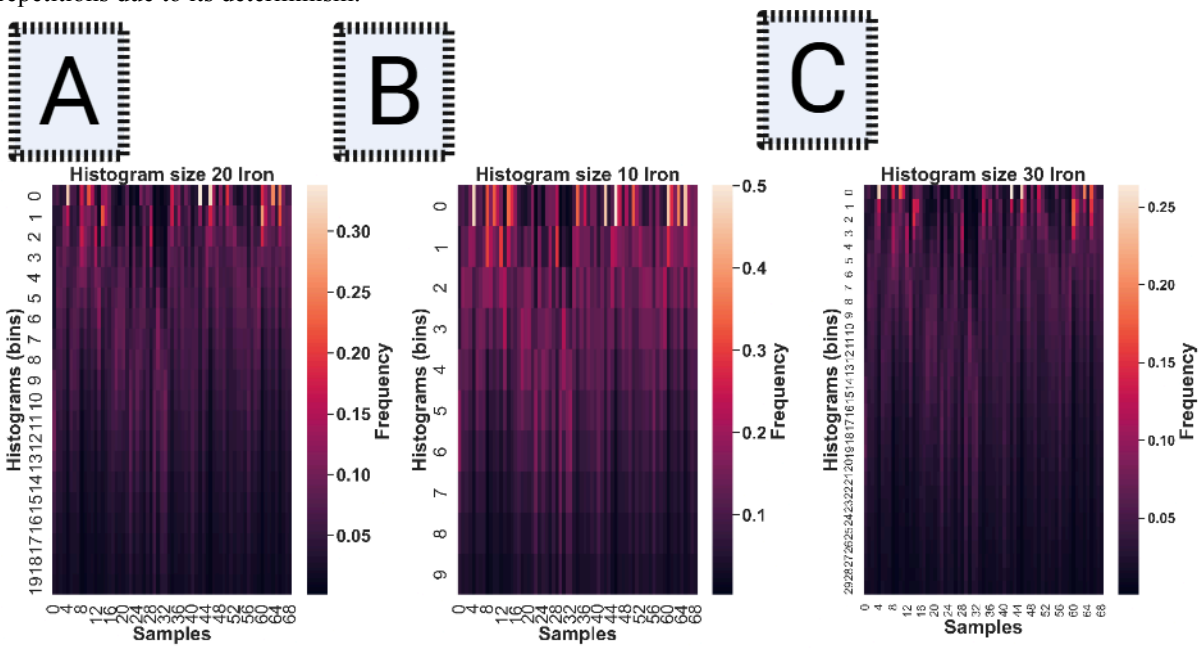

Figure S10. (**A**) Samples' tissue pixels after background and outlier removal and without Yeo-Johnson transformation represented in 20-bin histogram (**B**) Represented in 10-bin histogram (**C**) Represented in 30-bin histogram.

Sample ID	Magnesium	Iron	Copper	Zinc
Leap003	1 Tumor	1 Fibro with inflam	2 Tumor	1 Tumor
Leap009	1 Tumor with inflam 1 Tumor	2 Tumor with inflam 1 Tumor	2 Tumor with inflam 1 Tumor	
Leap013	1 Invasive	2 Tumor; 1 Fibro	1 Tumor with inflam 2 Tumor	1 Tumor
Leap019a		1 Fibro with inflam 2 Tumor	1 Necrosis	3 Tumor 1 Necrosis
Leap019b		2 Tumor	1 Necrosis	1 Tumor; 1 Necrosis
Leap023a		1 Tumor in fibrous	1 Tumor with fibro	1 Tumor with fibro
Leap023b	2 Inflam	1 Tumor in fibrous	1 Tumor with fibro	1 Tumor with fibro
Leap032a	1 Necrosis; 1 Inv	2 Necrosis; 3 Tumor	2 Necrosis; 2 Tumor	1 Normal; 1 Necrosis
Leap042a	2 Inflam with tumor 1 Fibrous stroma	1 Tumor with inflam; 1 Fibrous	1 Tumor with inflam; 1 Fibrous	1 Inflam
Leap043a	1 Fibrous tissue with inflam 1 Tumor with inflam in fibrous stroma 1 Fibrous tissue	1 Tumor with inflam in fibrous stroma 1 Fibrous tissue	1 Tumor with inflam in fibrous stroma	1 Fibrous with inflam 1 Tumor with inflam in fibrous stroma
Leap064a	1 Normal fibrous 1 Fibrous with inflam 2 Tumor 1 Necrosis	1 Normal fibro 1 Fibrous with inflam 2 Tumor 1 Necrosis	1 Normal fibro 1 Fibrous tissue with inflam 2 Tumor 1 Necrosis	1 Normal fibro 1 Fibrous tissue with inflam 2 Tumor
Leap066a	1 Tumor 1 Tumor with inflam	1 Tumor 1 Tumor with inflam	1 Tumor 1 Tumor with inflam	1 Tumor 1 Tumor with inflam
Leap068a	1 Tumor with inflam 1 Tumor	1 Tumor with inflam 1 Tumor	1 Tumor with inflam 1 Tumor	1 Tumor with inflam 1 Tumor
Leap069a	1 Tumor with inflam 2 Tumor	2 Tumor; 2 Fibrous 1 Inflam	1 Tumor with inflam 2 Tumor	1 Tumor with inflam 2 Tumor
Leap073a	3 Tumor	2 Tumor 1 Tumor with inflam	1 Necrosis 2 Tumor 1 Tumor with inflam	1 Necrosis 4 Tumor 1 Tumor with inflam
Leap077a	3 Tumor with inflam	2 Tumor with inflam 1 Tumor within fibrous	2 Tumor with inflam 1 Tumor within fibrous	2 Tumor with inflam 1 Tumor within fibrous
Leap080a	1 Tumor; 2 DCIS	1 Fibrous 1 Fibrous with inflam 2 DCIS	1 Tumor; 2 DCIS	1 Tumor
Leap082a	2 Fibrous with inflam 3 Tumor with inflam	2 Fibrous with inflam	1 Fibrous with inflam	3 Tumor with inflam

		2 Infalm with fibrous	3 Tumor with inflam	
Leap087a	5 Tumor 4 Inflam 1 Tumor with inflam 1 Tumor in blood vessel	1 Fibrous 2 Tumor 1 Necrotic tumor	1 Necrotic tumor 1 Tumor with inflam	4 Tumor 2 Inflam 1 Tumor with inflam
Leap090a	1 Tumor; 2 DCIS	1 Tumor 3 DCIS	1 Tumor; 4 DCIS	1 Tumor; 2 DCIS
Leap105a	1 Tumor; 1 Inflam	1 Tumor with inflam 1 Inflam at edge of tumor 2 Fibrous stroma in the tumor	2 Tumor; 1Inflam	2 Tumor

Table S1. Table of 21 samples with detailed pathologist annotation (like Fig. S7 right). For each sample we counted pathologist annotations with clear overlap of hotspot regions per metal (like Fig. S3-S6).

Bibliography

[1] N. Abbaspour, R. Hurrell, and R. Kelishadi, “Review on iron and its importance for human health,” *J. Res. Med. Sci. Off. J. Isfahan Univ. Med. Sci.*, vol. 19, no. 2, p. 164, 2014.

[2] O. R. Avram, G. Caragea, and C. A. Varzaru, “Copper and its role in the human body–the importance of establishing copper concentrations in the body,” *Romanian J*, vol. 124, no. 2, p. 254, 2021.

[3] A. Takeda, “Movement of zinc and its functional significance in the brain,” *Brain Res. Rev.*, vol. 34, no. 3, pp. 137–148, 2000.

[4] A. M. Al Alawi, S. W. Majoni, and H. Falhammar, “Magnesium and human health: perspectives and research directions,” *Int. J. Endocrinol.*, vol. 2018, no. 1, p. 9041694, 2018.

[5] A. Aggarwal and M. Bhatt, “Update on Wilson disease,” *Int. Rev. Neurobiol.*, vol. 110, pp. 313–348, 2013.

[6] E. M. Walker and S. M. Walker, “Effects of iron overload on the immune system,” *Ann. Clin. Lab. Sci.*, vol. 30, no. 4, pp. 354–365, 2000.

[7] L. Fouani, S. V. Menezes, M. Paulson, D. R. Richardson, and Z. Kovacevic, “Metals and metastasis: exploiting the role of metals in cancer metastasis to develop novel anti-metastatic agents,” *Pharmacol. Res.*, vol. 115, pp. 275–287, 2017.

[8] L. Chen *et al.*, “Zonated Copper-Driven Breast Cancer Progression Countered by a Copper-Depleting Nanoagent for Immune and Metabolic Reprogramming,” *Adv. Sci.*, vol. 12, no. 20, p. 2412434, 2025, doi: 10.1002/advs.202412434.

[9] Y. Xu, A. Reheman, and W. Feng, “Recent research progress on metal ions and metal-based nanomaterials in tumor therapy,” *Front. Bioeng. Biotechnol.*, vol. 13, p. 1550089, Feb. 2025, doi: 10.3389/fbioe.2025.1550089.

[10] Y. Chen, C. Li, M. Li, and B. Han, “Roles of Copper Transport Systems Members in Breast Cancer,” *Cancer Med.*, vol. 13, no. 24, p. e70498, Dec. 2024, doi: 10.1002/cam4.70498.

[11] L. Finney, S. Vogt, T. Fukai, and D. Glesne, “Copper and angiogenesis: unravelling a relationship key to cancer progression,” *Clin. Exp. Pharmacol. Physiol.*, vol. 36, no. 1, pp. 88–94, 2009.

[12] M. P. Waalkes, D. A. Fox, J. C. States, S. R. Patierno, and M. J. McCabe Jr, “Metals and disorders of cell accumulation: modulation of apoptosis and cell proliferation,”

Toxicol. Sci., vol. 56, no. 2, pp. 255–261, 2000.
[13] H. Zheng *et al.*, “A copper complex that combats triple negative breast cancer by restraining angiogenesis,” *Dalton Trans.*, vol. 52, no. 22, pp. 7626–7634, Jun. 2023, doi: 10.1039/D3DT00738C.
[14] M. Y. Hsu, E. Mina, A. Roetto, and P. E. Porporato, “Iron: an essential element of cancer metabolism,” *Cells*, vol. 9, no. 12, p. 2591, 2020.
[15] O. Karginova *et al.*, “Inhibition of copper transport induces apoptosis in triple-negative breast cancer cells and suppresses tumor angiogenesis,” *Mol. Cancer Ther.*, vol. 18, no. 5, pp. 873–885, 2019.
[16] S. Alam and S. L. Kelleher, “Cellular mechanisms of zinc dysregulation: a perspective on zinc homeostasis as an etiological factor in the development and progression of breast cancer,” *Nutrients*, vol. 4, no. 8, pp. 875–903, 2012.
[17] P. M. V. Mendes *et al.*, “Magnesium in breast cancer: what is its influence on the progression of this disease?,” *Biol. Trace Elem. Res.*, vol. 184, pp. 334–339, 2018.
[18] I. Sharma, “ICP-OES: An advance tool in biological research,” *Open J Env. Biol*, vol. 5, no. 1, pp. 027–033, 2020.
[19] O. Toker *et al.*, “Determination of Se, Cr, Mn, Zn, Co, Na, and K in blood samples of breast cancer patients to investigate their variation using ICP-MS and ICP-OES,” *At. Spectrosc.*, vol. 40, 2019.
[20] B. Czerny, K. Krupka, M. Ożarowski, and A. Seremak-Mrozikiewicz, “Screening of trace elements in hair of the female population with different types of cancers in Wielkopolska region of Poland,” *Sci. World J.*, vol. 2014, no. 1, p. 953181, 2014.
[21] A. Ghezzi, M. Aceto, C. Cassino, E. Gabano, and D. Osella, “Uptake of antitumor platinum (II)-complexes by cancer cells, assayed by inductively coupled plasma mass spectrometry (ICP-MS),” *J. Inorg. Biochem.*, vol. 98, no. 1, pp. 73–78, 2004.
[22] J. S. Becker, A. Matusch, and B. Wu, “Bioimaging mass spectrometry of trace elements–recent advance and applications of LA-ICP-MS: a review,” *Anal. Chim. Acta*, vol. 835, pp. 1–18, 2014.
[23] R. G. de Vega, M. L. Fernández-Sánchez, J. Pisonero, N. Eiró, F. J. Vizoso, and A. Sanz-Medel, “Quantitative bioimaging of Ca, Fe, Cu and Zn in breast cancer tissues by LA-ICP-MS,” *J. Anal. At. Spectrom.*, vol. 32, no. 3, pp. 671–677, 2017.
[24] D. Riesop, A. V. Hirner, P. Rusch, and A. Bankfalvi, “Zinc distribution within breast cancer tissue: A possible marker for histological grading?,” *J. Cancer Res. Clin. Oncol.*, vol. 141, pp. 1321–1331, 2015.
[25] P. Rusch, A. V. Hirner, O. Schmitz, R. Kimmig, O. Hoffmann, and M. Diel, “Zinc distribution within breast cancer tissue of different intrinsic subtypes,” *Arch. Gynecol. Obstet.*, vol. 303, pp. 195–205, 2021.
[26] S. Escudero-Cernuda *et al.*, “Quantitative distribution of essential elements and non-essential metals in breast cancer tissues by LA-ICP-TOF–MS,” *Anal. Bioanal. Chem.*, vol. 417, no. 2, pp. 361–371, 2025.
[27] “Delta Tissue,” Wellcome Leap: Unconventional Projects. Funded at Scale. Accessed: Oct. 06, 2025. [Online]. Available: https://wellcomeleap.org/delta-tissue/
[28] I.-K. Yeo and R. A. Johnson, “A new family of power transformations to improve normality or symmetry,” *Biometrika*, vol. 87, no. 4, pp. 954–959, 2000.
[29] A. Górska, A. Markiewicz-Gospodarek, M. Trubalski, M. Żerebiec, J. Poleszak, and R. Markiewicz, “Assessment of the Impact of Trace Essential Metals on Cancer Development,” *Int. J. Mol. Sci.*, vol. 25, no. 13, p. 6842, 2024.
[30] S. Blockhuys *et al.*, “Defining the human copper proteome and analysis of its expression variation in cancers,” *Metallomics*, vol. 9, no. 2, pp. 112–123, 2017.
[31] Y. Liu, J. Wang, and M. Jiang, “Copper-related genes predict prognosis and characteristics of breast cancer,” *Front. Immunol.*, vol. 14, Apr. 2023, doi: 10.3389/fimmu.2023.1145080.
[32] Y. Li *et al.*, “Identification and validation of a copper homeostasis-related gene signature for the predicting prognosis of breast cancer patients via integrated bioinformatics analysis,” *Sci. Rep.*, vol. 14, no. 1, p. 3141, Feb. 2024, doi:

10.1038/s41598-024-53560-9.
[33] G. MacDonald *et al.*, “Memo is a copper-dependent redox protein with an essential role in migration and metastasis,” *Sci. Signal.*, vol. 7, no. 329, pp. ra56–ra56, 2014.
[34] Y. Bengtsson *et al.*, “Serum copper, zinc and copper/zinc ratio in relation to survival after breast cancer diagnosis: A prospective multicenter cohort study,” *Redox Biol.*, vol. 63, p. 102728, Jul. 2023, doi: 10.1016/j.redox.2023.102728.
[35] M. Vogel-González, D. Musa-Afaneh, P. Rivera Gil, and R. Vicente, “Zinc favors triple-negative breast cancer’s microenvironment modulation and cell plasticity,” *Int. J. Mol. Sci.*, vol. 22, no. 17, p. 9188, 2021.
[36] A. Vikal, R. Maurya, P. Patel, R. K. Narang, and B. D. Kurmi, “From resistance to Response: Metallic nanoparticles as game changers in triple negative breast cancer therapy,” *J. Drug Deliv. Sci. Technol.*, vol. 113, p. 107322, Nov. 2025, doi: 10.1016/j.jddst.2025.107322.
[37] A. F. Lagalante, “Atomic absorption spectroscopy: A tutorial review,” *Appl. Spectrosc. Rev.*, vol. 34, no. 3, pp. 173–189, 2004.
[38] E. Dipietro *et al.*, “Comparison of an inductively coupled plasma-atomic emission spectrometry method for the determination of calcium, magnesium, sodium, potassium, copper and zinc with atomic absorption spectroscopy and flame photometry methods,” *Sci. Total Environ.*, vol. 74, pp. 249–262, 1988.
[39] S. C. Wilschefski and M. R. Baxter, “Inductively coupled plasma mass spectrometry: introduction to analytical aspects,” *Clin. Biochem. Rev.*, vol. 40, no. 3, p. 115, 2019.
[40] K. G. Daniel, D. Chen, S. Orlu, Q. C. Cui, F. R. Miller, and Q. P. Dou, “Clioquinol and pyrrolidine dithiocarbamate complex with copper to form proteasome inhibitors and apoptosis inducers in human breast cancer cells,” *Breast Cancer Res.*, vol. 7, pp. 1–12, 2005.
[41] P. A. Doble and G. L. G. Miklos, “Distributions of manganese in diverse human cancers provide insights into tumour radioresistance,” *Metallomics*, vol. 10, no. 9, pp. 1191–1210, 2018.
[42] P. Thölke *et al.*, “Class imbalance should not throw you off balance: Choosing the right classifiers and performance metrics for brain decoding with imbalanced data,” *NeuroImage*, vol. 277, p. 120253, Aug. 2023, doi: 10.1016/j.neuroimage.2023.120253.
[43] D. Freedman and P. Diaconis, “On the histogram as a density estimator: L 2 theory,” *Z. Für Wahrscheinlichkeitstheorie Verwandte Geb.*, vol. 57, no. 4, pp. 453–476, 1981.
[44] L. J. Castellanos-García, S. G. Elci, and R. W. Vachet, “Reconstruction, analysis, and segmentation of LA-ICP-MS imaging data using Python for the identification of sub-organ regions in tissues,” *Analyst*, vol. 145, no. 10, pp. 3705–3712, 2020.
[45] A. Oros-Peusquens, A. Matusch, J. S. Becker, and N. Shah, “Automatic segmentation of tissue sections using the multielement information provided by LA-ICP-MS imaging and k-means cluster analysis,” *Int. J. Mass Spectrom.*, vol. 307, no. 1–3, pp. 245–252, 2011.
[46] J. L. Beard and J. R. Connor, “Iron status and neural functioning,” *Annu. Rev. Nutr.*, vol. 23, no. 1, pp. 41–58, 2003.
[47] D. Sappey-Marinier *et al.*, “Alterations in brain phosphorus metabolite concentrations associated with areas of high signal intensity in white matter at MR imaging.,” *Radiology*, vol. 183, no. 1, pp. 247–256, Apr. 1992, doi: 10.1148/radiology.183.1.1549681.
[48] C. M. Elitt, C. J. Fahrni, and P. A. Rosenberg, “Zinc homeostasis and zinc signaling in white matter development and injury,” *Neurosci. Lett.*, vol. 707, p. 134247, Aug. 2019, doi: 10.1016/j.neulet.2019.05.001.
[49] J. Osborne, “Notes on the use of data transformations,” *Pract. Assess. Res. Eval.*, vol. 8, no. 1, Art. no. 1, Jan. 2002, doi: 10.7275/4vng-5608.
[50] C. FENG *et al.*, “Log-transformation and its implications for data analysis,” *Shanghai Arch. Psychiatry*, vol. 26, no. 2, pp. 105–109, Apr. 2014, doi: 10.3969/j.issn.1002-0829.2014.02.009.
[51] T. Marchand, B. Muzellec, C. Béguier, J. Ogier du Terrail, and M. Andreux,

"SecureFedYJ: a safe feature Gaussianization protocol for Federated Learning," *Adv. Neural Inf. Process. Syst.*, vol. 35, pp. 36585–36598, Dec. 2022.
[52] R. P. Brent, *Algorithms for Minimization Without Derivatives*. Courier Corporation, 2013.
[53] M. V. Babak and D. Ahn, "Modulation of Intracellular Copper Levels as the Mechanism of Action of Anticancer Copper Complexes: Clinical Relevance," *Biomedicines*, vol. 9, no. 8, Art. no. 8, Aug. 2021, doi: 10.3390/biomedicines9080852.
[54] X. Li, Z. Ma, and L. Mei, "Cuproptosis-related gene SLC31A1 is a potential predictor for diagnosis, prognosis and therapeutic response of breast cancer," *Am. J. Cancer Res.*, vol. 12, no. 8, pp. 3561–3580, Aug. 2022.
[55] J. Fan *et al.*, "The relationship between serum level of copper and ceruloplasmin and pathologic and clinical characteristics in early breast cancer patients.," *J. Clin. Oncol.*, vol. 36, no. 15_suppl, pp. e13504–e13504, May 2018, doi: 10.1200/JCO.2018.36.15_suppl.e13504.
[56] F. Chen *et al.*, "Ceruloplasmin correlates with immune infiltration and serves as a prognostic biomarker in breast cancer," *Aging*, vol. 13, no. 16, pp. 20438–20467, Aug. 2021, doi: 10.18632/aging.203427.
[57] K. Geraki, M. J. Farquharson, and D. A. Bradley, "Concentrations of Fe, Cu and Zn in breast tissue: a synchrotron XRF study," *Phys. Med. Biol.*, vol. 47, no. 13, p. 2327, Jun. 2002, doi: 10.1088/0031-9155/47/13/310.
[58] N. Kagara, N. Tanaka, S. Noguchi, and T. Hirano, "Zinc and its transporter ZIP10 are involved in invasive behavior of breast cancer cells," *Cancer Sci.*, vol. 98, no. 5, pp. 692–697, 2007, doi: 10.1111/j.1349-7006.2007.00446.x.
[59] Z. Qu *et al.*, "A Systematic Study on Zinc-Related Metabolism in Breast Cancer," *Nutrients*, vol. 15, no. 7, p. 1703, Mar. 2023, doi: 10.3390/nu15071703.

תקציר

למתכות יש תפקיד קריטי בביולוגיה של הסרטן, אך בשיטות אנליטיות הקיימות חסר כימות מרחבי ולעיתים קרובות הן מסתמכות על מדידות גלובליות או תצפיות איכותניות. בתזה זו, אני מציג שיטה חישובית אוטומטית לניתוח כמותי של מתכות במרחב, ויישמתי אותה בחיזוי תגובה לטיפול כימותרפי ניאו-אדג'ובנטי (NACT) בקרב חולות סרטן שד משולש-שלילי (Triple Negative Breast Cancer). באמצעות דימות בשיטת ספקטרומטריית מסת פלזמה בצימוד אינדוקטיבי מבוססת אבלציית לייזר (Laser Ablation Inductively Coupled Plasma Mass Spectrometry) שמדדה התפלגות מרחביות של מגנזיום, ברזל, נחושת ואבץ מדגימות רקמת ביופסיה שנלקחו לפני הטיפול, השיטה החישובית שלי ממירה קריאות מתכתיות מרחביות לייצוג מבוסס היסטוגרמה המשמש כקלט למודל החיזוי. אני מדגים כי ההתפלגויות המרחביות של כל ארבעת המתכות מכילות מידע לחיזוי תגובה לטיפול. התוצאה המרכזית היא סינגל החיזוי נמצא ב"אזורים חמים" (hotspots) - אזורים ברקמה בעלי ריכוזי מתכות גבוהים, המזוהים באמצעות שילוב מידע מכמה מתכות. אזורים חמים אלו חופפים באופן חלקי לאנוטציות פתולוגיות כגון גידול סרטני (tumor), דלקת מרובה בתאי מערכת חיסונית (inflammation) וסטרומה סיבית (fibrous stroma), דבר המצביע על כך שהם מייצגים אזורים בעלי משמעות ביולוגית. בעוד שמודלים המבוססים על מתכות בודדות הם בעלי יכולת חיזוי, אנחנו אני מדגים כי שאיסוף התחזיות שלהם משפר באופן משמעותי את סיווג תגובת המטופלת. ממצא זה מדגיש את הערך של שילוב מידע מרחבי וממספר מתכות לחשיפת סמנים ביולוגים לתגובה לכימותרפיה ב TNBC. לסיכום, תזה זו מספקת שיטה חישובית לניתוח כמותי של מתכות במרחב בדימות ביולוגי, ומדגימה את חשיבותם של אזורים חמים רב מתכתיים כאזורים אינפורמטיביים לחיזוי תגובה לטיפול.

אוניברסיטת בן-גוריון בנגב
הפקולטה למדעי המחשב והמידע
התכנית להנדסת מערכות מידע

ניתוח כמותי של ביו-דימות מתכתי בחולות סרטן שד משולש שלילי

חיבור זה מהווה חלק מהדרישות לקבלת תואר מוסמך במדעים (M.Sc)

מרק אוליטין

בהנחיית **פרופ' אסף זריצקי וד"ר אורית קליפר גרוס**

חתימת המחבר:  תאריך: 01/10/2025

אישור מנחה:  תאריך: 01/10/2025

אישור יו"ר ועדת תואר שני מחלקתית: _____ תאריך: _____

אוקטובר 2025

אוניברסיטת בן-גוריון בנגב
הפקולטה למדעי המחשב והמידע
התכנית להנדסת מערכות מידע

ניתוח כמותי של ביו-דימות מתכתי בחולות סרטן שד משולש שלילי

חיבור זה מהווה חלק מהדרישות לקבלת תואר מוסמך במדעים (M.Sc)

מרק אוליטין

בהנחיית **פרופ' אסף זריצקי וד"ר אורית קליפר גרוס**

אוקטובר 2025